LOW TEMPERATURE MELTING POINT METALS FOR HOT MEMS ELECTRICAL SWITCHING

By

YOONKAP KIM

A thesis submitted in partial fulfillment of
the requirements for the degree of

MASTER OF SCIENCE IN MATERIAL SCIENCE AND ENGINEERING

WASHINGTON STATE UNIVERSITY
School of Mechanical and Materials Engineering

December 2007

To the Faculty of Washington State University:

The members of the Committee appointed to examine the thesis of YOONKAP KIM find it satisfactory and recommend that it be accepted.

_____

Chair

_____

_____

_____

ACKNOWLEDGEMENT

First I would like to thank my advisor Dr. David F. Bahr for allowing me the opportunity to work on this research. I am very fortunate because he has continually provided the right balance of guidance and autonomy to help me develop into a better engineer. Even though I had not good English skills, he always advised to me with patient. If I do not have his patient help, I would not have completed this research. I also would like to thank Dr. Cill D. Richards and Dr. David Field for additional support, encouragement, and guidance.

I acknowledge my office mates and group members, Zach Seeley, Mohammad Al-Khedher, Ali A Zbib, Jeong Hyun Cho, Tae-Jin Kim, Ryan Johnson, and Katerina Bellou, for their help and encouragement. Thanks to their patient support, my English skills have improved a lot; this will be a life precious treasure. I also appreciate my best friend ChanGil Jeong because he always encourage me and pray for me.

Finally, I thank my Lord for His love. I would not have completed my work without His guidance. I also appreciate my parents, Gueiim Na and Myungsik Kim for providing me with encouragement and financial support during my research. I would like to thank my wife Wonmi Choi and my daughter Lauren Hayul Kim for cheering up and supporting everything to me. I am very fortunate that I could do this research in Pullman at Washington State University.

LOW TEMPERATURE MELTING POINT METALS FOR

HOT MEMS ELECTRICAL SWITCHING

Abstract

by Yoonkap Kim, M.S.

Washington State University

DECEMBER 2007

Chair: David F. Bahr

This thesis presents a method to overcome the mechanical and chemical problems of liquid mercury MEMS electrical switches by using Gallium or Tin, which can be used as solid metal droplets for switches. To understand the structure of Gallium (Ga) and Tin (Sn) micro-droplets for switching operations, the micro-droplets were deposited on the fabricated samples by electroplating, and the behavior is investigated by characterizing the macro structure, adhesion, hardness, and electrical performance of low melting temperature droplets in MEMS structures.

The amount of the reacted micro-droplets of Sn and Ga with W was affected by the size of silicon dioxide (SiO_2) hole and tungsten (W) target, and thermal reflow time and temperature. The adhesion of the Ga droplet was investigated with contact angles between the droplet and the W dot in the fabricated sample. The contact angles of the deposited Ga droplet were 67.8˚ and 56˚, so it was shown that the Ga droplet had good

adhesion with W. The measured resistivity of the Ga droplet was 1.128 x 10^{-5} Ω cm. This value was similar to the theoretical value (1.00 x 10^{-5} Ω cm) for Ga, and suggests that the electrodeposited Ga will be suitable for a solid MEMS switch. The hardness of the Ga droplet was obtained with the micro Vickers hardness test, and was 17.2 HV. This suggests a maximum applied stress of 60 MPa can be applied to each droplet in the current configuration.

TABLE OF CONTENTS

LIST OF FIGURES

LIST OF TABLES

CHAPTER 1

INTRODUCTION

1.1 MOTIVATION FOR LOW TEMPERATURE MELTING POINT METALS FOR HOT MICROELECTROMECHANICAL SYSEMS (MEMS) ELECTRICAL SWITCH

Various types of micromechanical switches have been introduced since the technologies of microelectromechanical systems (MEMS) were developed in 1980s because of functional advantages of micromechanical switches [1-5]. These micromechanical switches show some benefits such as a wide operating temperature range, radiation insensibility, and a high on-off impedance ratio. Almost all micromechanical switches have been designed with solid-to-solid contacts [6]. Micromechanical switches have various problems such as contact bounce, noise, high contact resistance, slow rise times, and a short operational lifetime due to mechanical wear and tear. It has been suggested that these problems can be solved by liquid metal because it shows low contact resistance and a fast signal rise time, and can reduce wear and tear by its liquid phase [7].

MEMS switches can include both electrical and thermal switches. In the concept of electrical switches, the MEMS switches are typically operated through electrostatic attraction of a membrane or beam to electrodes on the substrate [8]. The principal operation of a conventional MEMS switch is explained in the figure 1.1. When DC voltage is applied to the driving electrodes, the membrane is attracted to the electrodes. This situation is expressed as the on state of the switch, and the capacitance of the switch is large. The membrane return to the previous position when the voltage is decreased

below 30-40 V. This condition means that the state of the switch is off, and the capacitance is small [9,10].

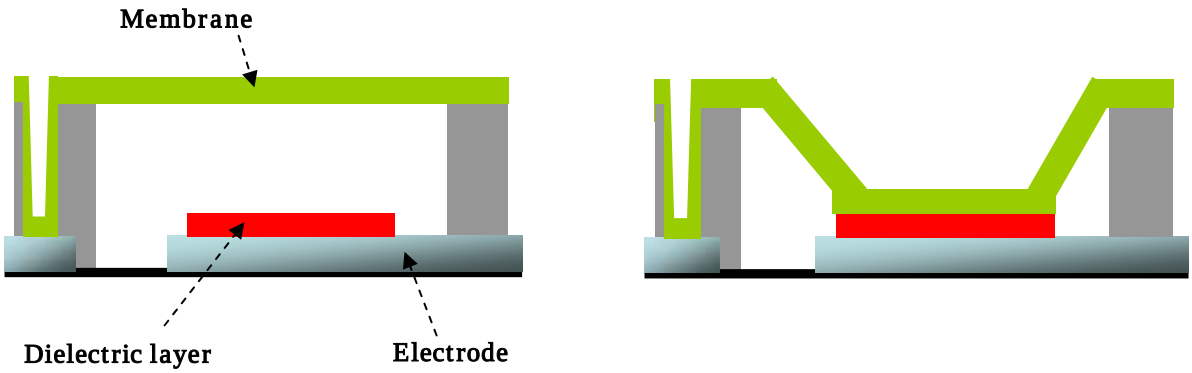

(a) Off state
: Open circuit,
Low capacitance

(b) On state
: Close circuit,
High capacitance

Figure 1.1 Schematic of the operation of MEMS switch.

For thermal switches MEMS device needs to have the ability to transfer heat efficiently but also perform at high frequency operation. Liquid metal can be used in the hot switch due to its characteristics such as conducting heat from heat source to the next membrane as shown in figure 1.2, using in micro gaps between a solid-to-solid contact, and overcoming mechanical wear by the switch operation at high frequency [11].

The representative liquid metal is mercury for thermal switches, but there is two limitations with the use of liquid mercury droplets. One of the limitations is the fact that mercury has a high toxicity and may be a significant health hazard through exposure [12]. The other reason is the mercury droplet can be difficult to use at high frequency (kHz) operation because it does not have good adhesion between liquid-solid contact. It means that high mechanical force should be applied to liquid mercury droplets for maintaining

the “ON” state in figure 1.2, and moreover the external force can be one factor to detach the droplets from the original positions [13]. Therefore, we need to find alternative metals to mercury for metal electrical and thermal switch.

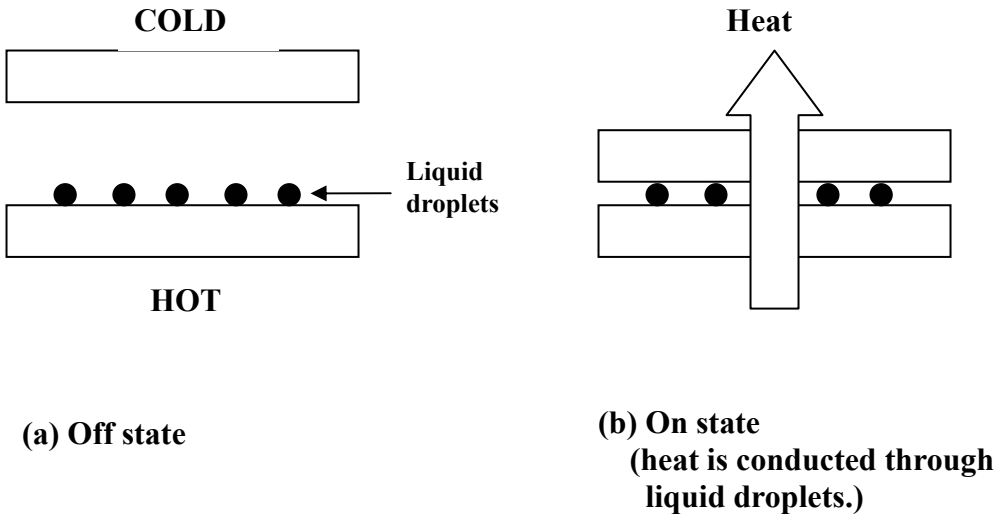

Figure 1.2 Schematic and operation of hot switch.

The aim of this research is to overcome the mechanical and chemical problems of the liquid mercury hot MEMS electrical switch by using Gallium and Tin which can be used as metal droplet for the MEMS switches. These metals have low melting temperatures, and so could be used as liquids at moderate temperatures, but could also be used as solids and then re-melted to “heal” a damaged switch. The structure of Gallium and Tin micro-droplets during fabrication needs to be understood if they are to be used instead of mercury micro- droplets. The behavior is investigated in this thesis by characterizing the structure, adhesion, hardness, and electrical performance of Gallium

and Tin droplets in MEMS structures.

1.2 THE CHARACTERISTICS OF THE LOW MELTING POINT LIQUID METALS

There are several pure low melting point liquid metals that could be used for MEMS switches such as gallium, mercury, sodium, potassium, phosphorous, and tin. Although the liquid metal alloys can be made with melting temperatures lower than the pure metals by the eutectics of the alloys, pure metals are usually used in the MEMS electrical switch. The reason is that the alloys do not always exhibit good electrical properties for most switching applications [14]. In this section, among these low melting point liquid metals, gallium, mercury, and tin will be discussed.

1.2.1 Properties of Gallium

Lecoq de Boisbaudran discovered gallium in 1875. Gallium has the second lowest melting point of any pure metal, and it has the widest temperature range in the liquid state. When gallium is slightly heated, it becomes liquid because its melting temperature is 29.78 ˚C. Pure gallium is soft with a Mohs' hardness of 1.5, and it is a white silver metal in the liquid state. When gallium is in the liquid state, it is difficult to distinguish from mercury, but has a specific gravity of about 6 and a greater viscosity than mercury [15-17]. The crystal-lattice of gallium is formed by diatomic molecules (a=2.47Å), and the crystal structure is orthorhombic. The density of solid gallium is 5.904 g/cm^3 while that of liquid gallium is 6.095 g/cm^3. When liquid gallium is solidified, the volume increases by 3.2%. This change is rarely observed in other metals but is true for water [17]. Liquid gallium wets most surfaces except graphite and Teflon, but the wetting of liquid gallium can be controlled by adding dilute hydrochloric acid to prevent wetting

[15]. Gallium has an advantage as a heat-conducting liquid because it has a high boiling point and a high thermal conductivity. The conductivity of liquid gallium is about twenty times greater than mercury. Gallium aggressively attacks most metals except tungsten and tantalum at any given temperature, so it can readily alloy with many metals [14, 17, 18]. Tungsten features are wettable by gallium, so when gallium is deposited on a substrate, tungsten can be used as target. The phase diagram of the gallium-tungsten binary alloy system is shown in figure 1.3 [19]. Table 1.1 exhibits the physical properties of gallium.

Atomic Number	**31**
Atomic Weight	**69.72 g/mol**
Melting Point	**29.78 °C**
Boiling Point	**2400 °C (approx.)**
Density of Solid	**5.904 g/ cm^3**
Resistivity	**1.00E-07 Ωm**
Thermal Conductivity (30°C)	**35 W/mK**
Heat of Fusion	**19.16 cal/g**
Specific Heat Capacity	**371 J/kgK**
Expansion of Freezing	**3.2 %**

Table 1.1 Physical properties of Gallium [11, 15]

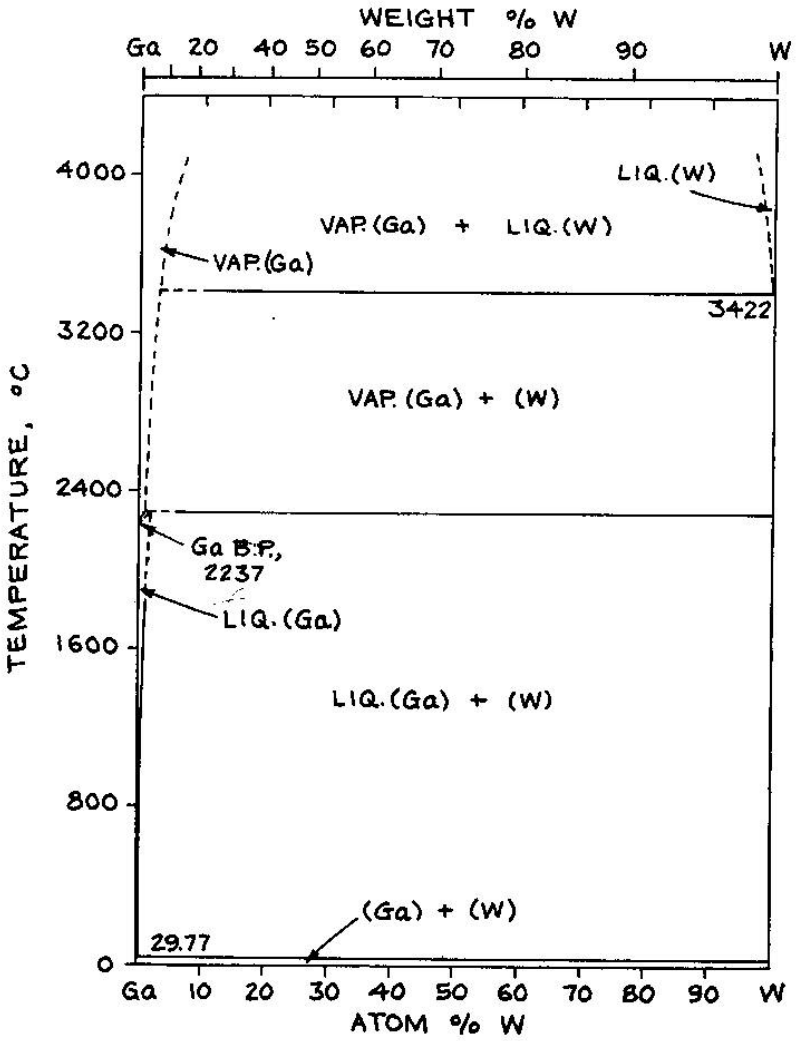

Figure 1.3 Phase diagram of the Ga-W binary alloy system [19].

1.2.2 Properties of mercury

Mercury has been studied since ancient times. Mercury is the only liquid metal at room temperatures because the melting point of mercury is -38.9°C [16]. Its boiling temperature is also low (356.6°C), so evaporation can be used for deposition of mercury. Mercury easily reacts with gold, so gold is used as target for nucleating mercury when mercury is deposited on the substrate. Figure 1.4 represents the phase diagram of the mercury-gold binary system [20].

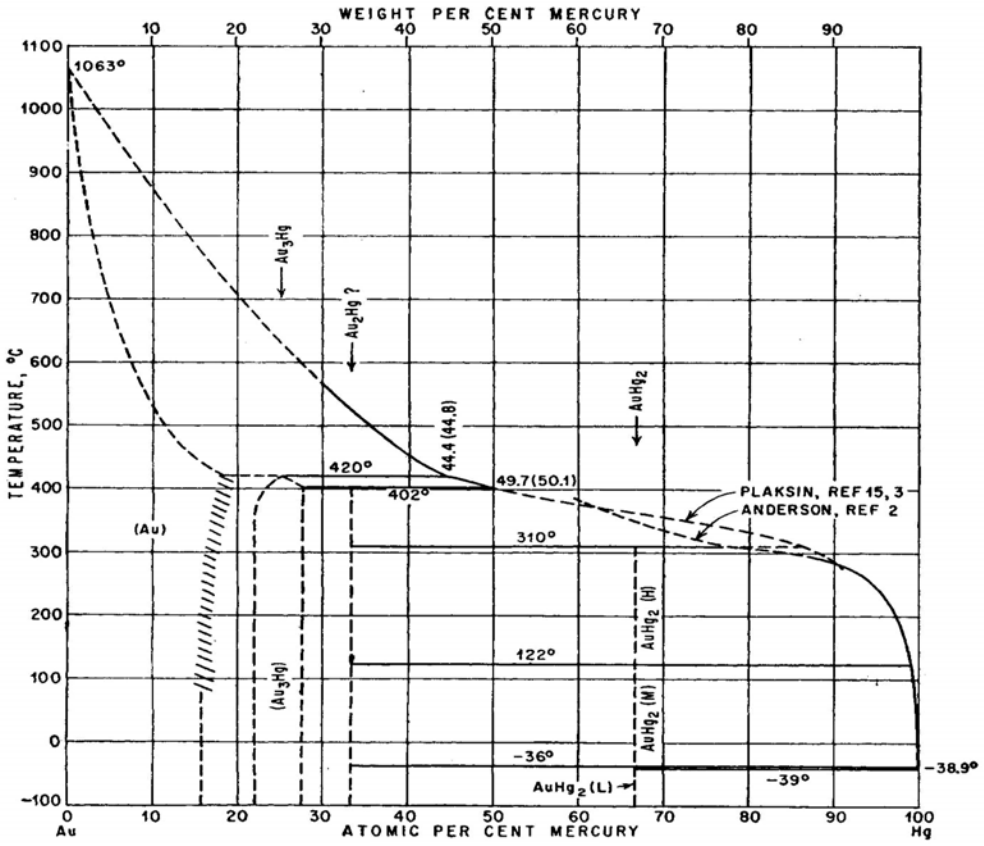

Figure 1.4 Phase diagram of the Au-Hg binary alloy system [20].

Mercury does not wet most surfaces, including glass, due to its high surface tension. The non-wetting behavior of mercury satisfies applications to require precise volume and dynamic control of the conducting medium [12]. Mercury is also used in barometers, manometers, and thermometers because it has high density and high rate of thermal expansion. However, mercury has health problems because of its toxicity. If a human is exposed to mercury, this can be caused harmful effects such as brain and kidney damage, nerve, lung and eye irritation, skin rashes, vomiting and diarrhea [16]. Therefore,

these harmful effects of mercury should be solved for safety using mercury in applications.

1.2.3 Properties of Tin

Tin is a soft, silvery-white metal, malleable, and ductile, and has highly crystalline structure. Its melting point is 232˚C. This melting temperature is comparatively lower than other metals, but the boiling temperature of tin is high as 2270˚C [16]. Tin resists distilled sea water and soft tap water, but can be attacked by strong acids, acid salts, and alkalis. The element of tin has two allotropic forms. When tin is warmed, its color, phase, and structure change at 13.2°C from grey to white, from α-tin to β-tin, and from a cubic structure to a tetragonal structure. On the other hand, if the temperature is cooled below 13.2°C, tin changes slowly from white to grey, from β-tin to α-tin, and from a tetragonal structure to a cubic structure. This change depends on impurities, and if antimony or bismuth is added, the change can be prevented. The physical properties of tin are shown in table 1.2 [21].

Atomic Number	**50**
Atomic Weight	**118.69 g/mol**
Melting Point	**232 ˚C**
Boiling Point	**2270 ˚C (approx.)**
Density of Solid	**7.3 g/ cm^3**
Resistivity	**11E-08 Ωm**

Table 1.2 Physical properties of Tin

1.3 DEPOSITION TECHNIQUES

Deposition techniques will be identified and described in this section because the deposition techniques will impact the resulting micro droplet structure. In this chapter electroplating (electrochemical deposition), thermal evaporation, screen printing, and solder jet injection printing will be discussed among the viable techniques.

1.3.1 Electroplating (Electrochemical Deposition)

Electroplating is one of the most popular deposition techniques. Electroplating can be defined as the "electrodeposition of an adherent metallic coating upon an electrode for the purpose of securing a surface with properties of dimensions different from those of the basic metal [22]." The definition should include plating on nonconductors such as plastics. One key of electroplating is the adhesion between the plate and substrate because in electroplating the deposit is an essential part of the electroplating work, and it has to be anticipated that the materials, which are deposited, should adhere to the base metal during the useful life of the object [23]. The electroplating process physically consists of four parts, the external circuit, a negative electrode (cathode), plating solution, and a positive electrode (anode). The external circuit consists of a source of direct current, and transports the current to the plating tank, and associated instruments like voltmeters and ammeters. The voltage and current can be regulated by the external circuit at their appropriate values. The negative electrodes (cathodes) are the material to be plated, and are contacted with the current source in the plating solution. The cathode gets the electrons from the external circuit by chemical reaction, and then ions are combined with the electrons, so a byproduct is produced at the cathodes [24]. The byproduct often

includes metallic ions, but also H2 gas. The positive electrode (anode) is a conducting material, because the anode completes the circuit by giving up the electrons to the circuit. The cathode and the anode is electrically connected by physical contact to allow the electrons to flow from the anode to the cathode for chemical reaction. The plating solution is often aqueous, and can be represented as a liquid electrolyte. The electrolyte is also conductive for completing the circuit, and helping to move ions to cathode [24]. The general arrangement of the electroplating is represented by figure1.5.

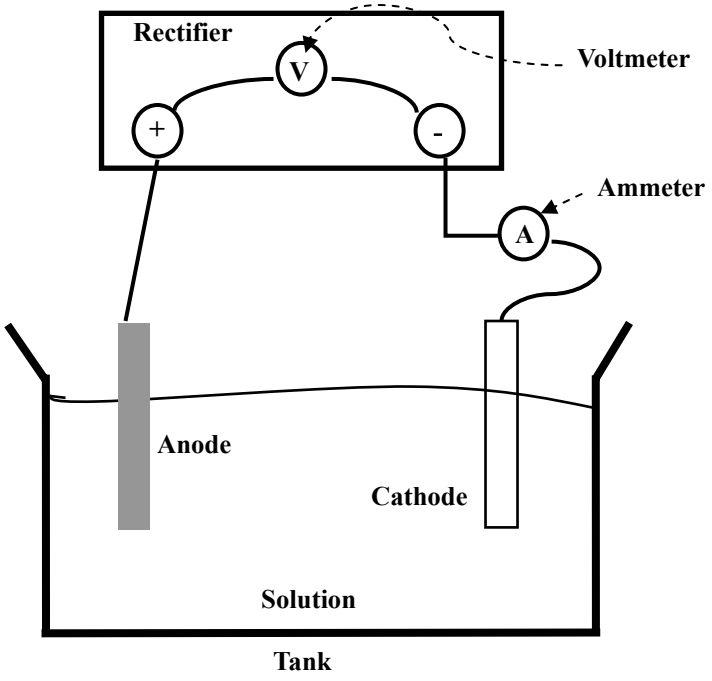

Figure 1.5 Schematic of electroplating layout.

The electroplated material may be usefully applied for protection, appearance, engineering or mechanical properties, or special surface properties.

1.3.2 Thermal Evaporation

Thermal evaporation is also one of the most popular and oldest deposition techniques for thin film materials. The principle is that the source, which is used for evaporation, is placed in a crucible, and then the crucible is heated up through a resistive element such as coil within vacuum chamber.

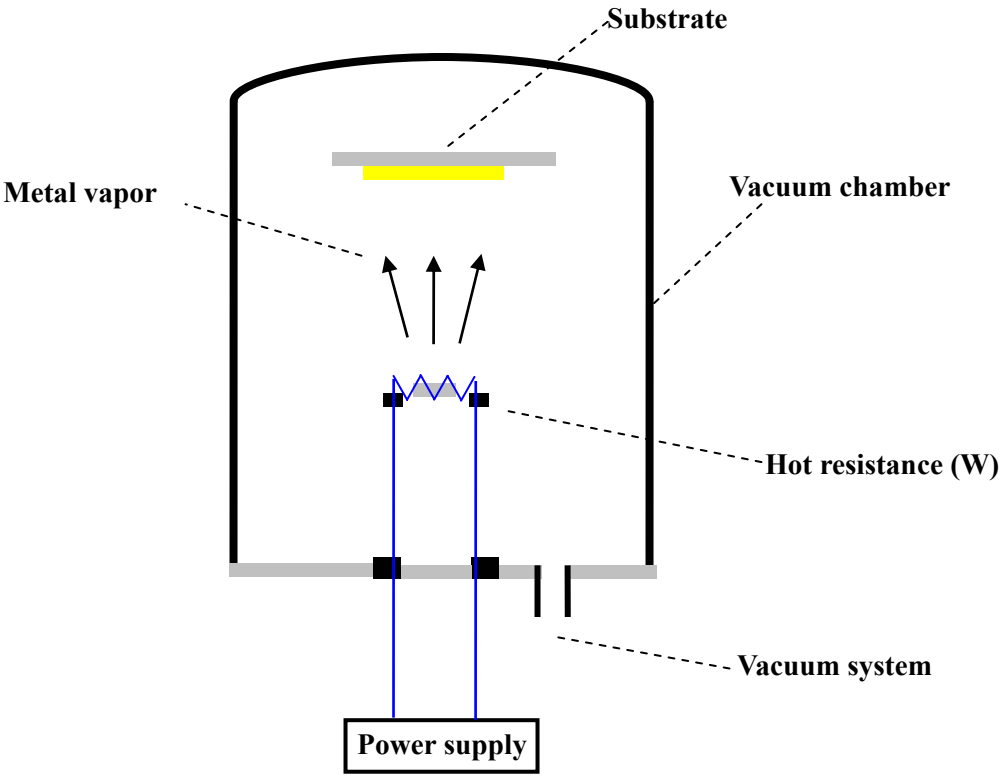

Figure 1.6 Schematic of the thermal evaporation

The source material is vaporized by sufficient heating power. The evaporated particles straightly transfer from the evaporation source towards the substrate because the

mean free path of vapor atoms is the same order as the vacuum chamber dimension, and then they are condensed on to the surface of the target substrate in the chamber. The average energy of vapor atoms is low for reaching the substrate surface, so a porous and little adherent material are often shown in the evaporated substrate surface [25, 26]. At this point the pressures in the chamber are about 10^{-5}- 10^{-6} Torr to avoid reaction between the vapor and atmosphere. In the thermal evaporation, evaporated materials are often metals in the solid state. Sometimes liquid state materials are used as the sources, but the success of deposition is very limited. Thermal evaporation does not have any limitation on the deposition process for pure elements alone. Moreover, alloy formation is also possible by evaporating constituent metals [27]. Figure 1.6 represents the schematic of the thermal evaporation.

1.3.3 Screen Printing

Screen printing is a simple and economical technique, and one of the oldest methods of basic electronics fabrication. The technology has been applied to robust electronic circuits, and miniaturized. Screen printing needs high viscosity fluid materials for deposition. The materials can be produced from an organic binder, a mixture of conductive particles, and solvent such as solder pastes [25]. The screen printing process is described by figure 1.7. The screen consists of a screen frame, a screen mesh, and a thick emulsion, which is placed on a stainless steel plate with patterned openings. In the process, and should be parallel to the target substrate with gap between the screen and the substrate. A squeegee is perpendicular to the surface of the screen and should move in the horizontal direction to be applied pressure on the screen and the substrate.

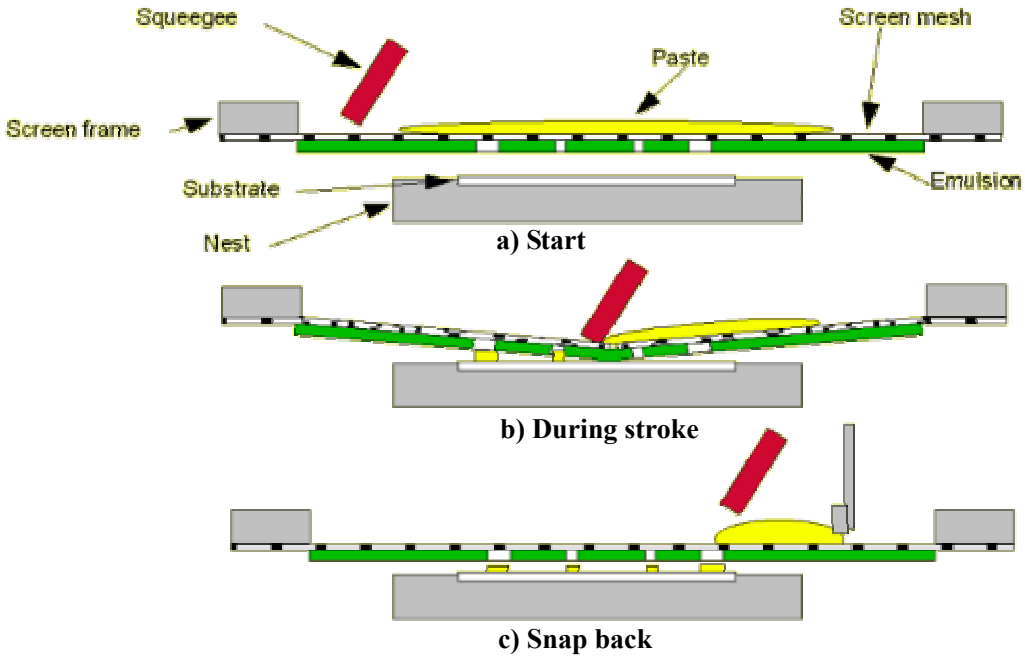

Figure 1.7 Schematic of the screen printing process [28]

The screen is subsequently deflected by the pressure and then the screen and the substrate are touched each other. The materials, which are the emulsified pastes, are deposited through the patterned openings and adhere to the substrate. The deposited materials are left on the substrate after the screen snaps back. The resolution of the screen printing depends on two main facts which are the fluid dynamics of the paste, and the opening geometries of the screen [25].

1.3.4 Solder Jet Injection Printing (or Thermal Inkjet)

Solder jet injection printing is one of the micromachined injector printing technologies. The concept of the solder jet injection printing is similar to ink-jet printing, because the solder jet injection systems consist of a piezoelectric micro transducer where produce the volumetric change of liquid solder in a chamber. Pressure and velocity are

applied to the liquid solder by the volumetric change, and then the liquid solder drops on the substrate from an orifice [29]. The delivering ability of the solder jet injection system is that 40-125μm solder drops can be transported at the rate of 2,000 drops per second, and the inject ability depends on the solder viscosity and surface tension [30, 31]. Therefore, the solder jet systems can be used for various applications such as flip-chip bonding, microelectronic manufacturing, and wafer bumping.

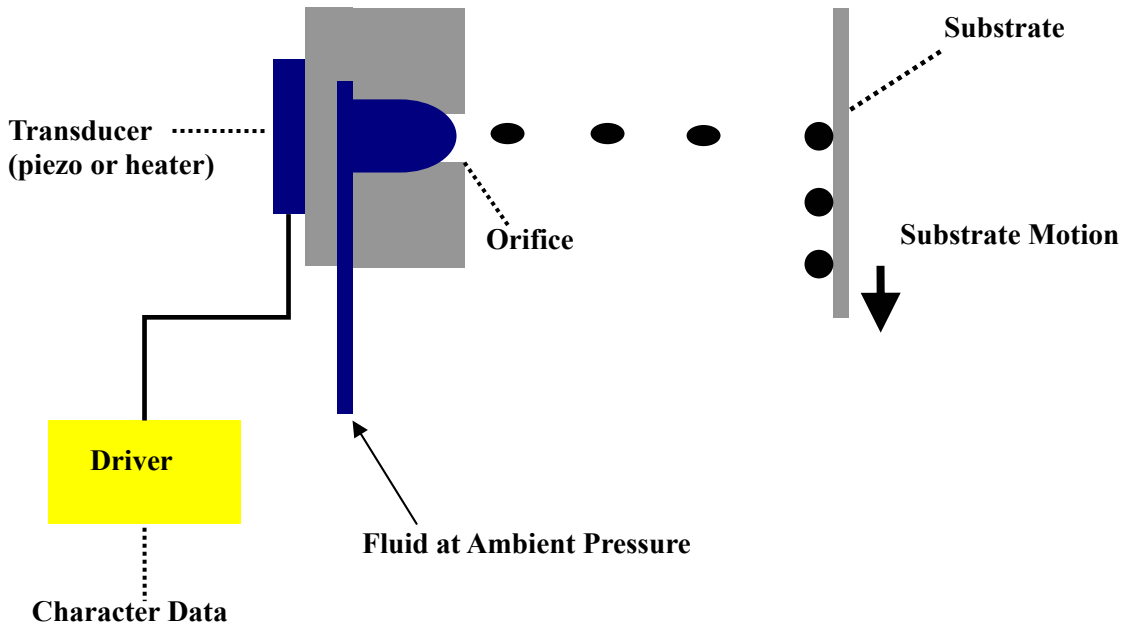

Figure 1.8 Schematic of Solder Jet Injection system [30]

The non-contact approach is one of the advantage processes of solder jet printing because in this case, the process does not need special tooling for specific run. Further, the data driven characteristic is real time process control, so the yields of the solder jet printing can be improved. The limitation of the system is higher manufacturing cost and

time to produce the results because specialized equipment is used for the system [30]. The schematic of solder jet injection system is represented by figure 1.8.

1.4 ADHESION AND WETTING OF THE INTERFACES

In the wettablility between a liquid and a solid, one of the most used concepts is intermolecular forces that occur between the liquid molecules and the interaction with the molecules of the solid. The molecules of the liquid tend to make a spherical geometry due to the intermolecular cohesive force. When a liquid is dropped on a solid surface, the final shape depends on the interfacial energies and adhesive force is generated by the molecular interaction of the molecules of the liquid and solid, and the liquid is spread on the surface by the adhesive force [32]. The wettability is determined by the contact angle, made by the balance between the liquid cohesive force and the adhesive force of the liquid-solid. Therefore, the contact angle is useful to predict wetting and adhesion properties of the solid. On the real surface the contact angle is affected by interfacial tensions, surface roughness, adsorbates on the surface, molecular orientation, chemical heterogeneity, swelling, and the composition of the material [33]. The contact angle is represented by Young's equation, and shown in figure 1.9.

$$\gamma_{LV} \cos\theta + \gamma_{SL} = \gamma_{SV} \tag{1.1}$$

where γ_{LV} is the surface tension of the liquid-vapor, γ_{SL} is the interfacial energy of the solid-liquid, γ_{SV} is the solid-vapor surface tension, and θ is the contact angle. The surface tension of the liquid-vapor can be explained as the resistance of the liquid to be increased in the surface area. If the contact angle θ is more than 90°, the liquid is non-wetting, and the liquid cohesive force is greater than the adhesive forces of the solid-liquid interface. On the other hand, if the contact angle θ is less than 90°, the liquid is said to be partial wetting, and the solid-liquid adhesive force is greater than the cohesive force of the liquid. If θ is equal to zero, one says the liquid completely wets the surface [34]. To measure the

contact angles a tangent line is placed to the sessile drop images at the point of contact with the surface, and then the contact angle is defined by average of 2 angles from the image [35].

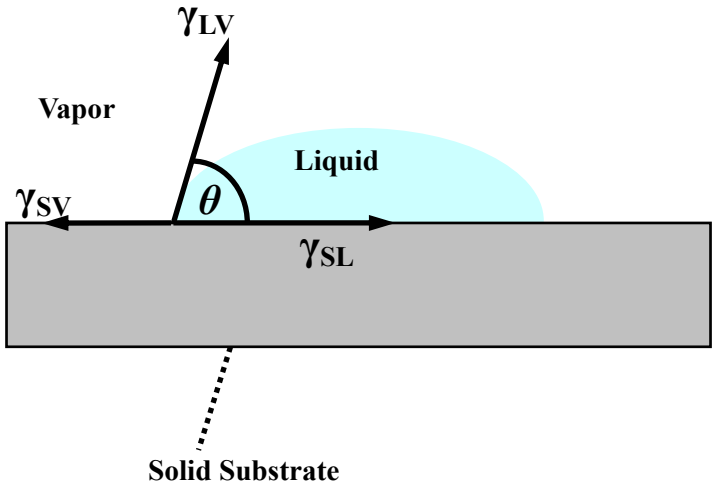

Figure 1.9 Schematic of a liquid drop on a substrate

If γ_{SL} and γ_{SV} are difficult to measure experimentally, the contact angle can be explained in a thermodynamics point of view [36]. In this case, the contact angle is expressed as:

$$\cos\theta = \frac{2W_a}{W_c} - 1 \qquad (1.2)$$

where W_a is the work of adhesion, and W_c is the work of cohesion. The work of adhesion may be represented as equation 1.3 because the surface energy, which is created before two materials are separated, is equal to the work of adhesion.

$$W_a = \gamma_{SV} + \gamma_{LV} - \gamma_{SL} \quad (1.3)$$

If the equation 1.3 is combined with the Young equation, it is defined by equation 1.4 [37, 38].

$$W_a = \gamma_{LV} (1 + \cos\theta) \quad (1.4)$$

The work of cohesion represents a measure of molecular interactions of a liquid for symmetric molecules, and equation 1.5 is obtained by the two liquid-vapor surfaces which are generated when a liquid drop is separated into two parts [36].

$$W_c = 2\gamma_{LV} \quad (1.5)$$

Therefore, the contact angle can be thermodynamically calculated by the value of the W_a and W_c.

CHAPTER 2

EXPERIMENTAL PROCEDURE

2.1 FABRICATION PROCESSES

The samples were fabricated from single side polished 3 inch diameter (100) silicon (Si) wafers. To increase the conductivity for electroplating and the electrical experiments, Boron (B) was used to dope the Si. B was diffused through the reaction of boron trioxide (B_2O_3) with Si at the Si wafer surface. In this case, a disk of boron nitride (B_3N_4) was utilized as a boron source. Silicon Dioxide (SiO_2) was grown as a thin (120-180μm) oxide layer on both sides of the wafer using a wet oxidation process after boron doping.

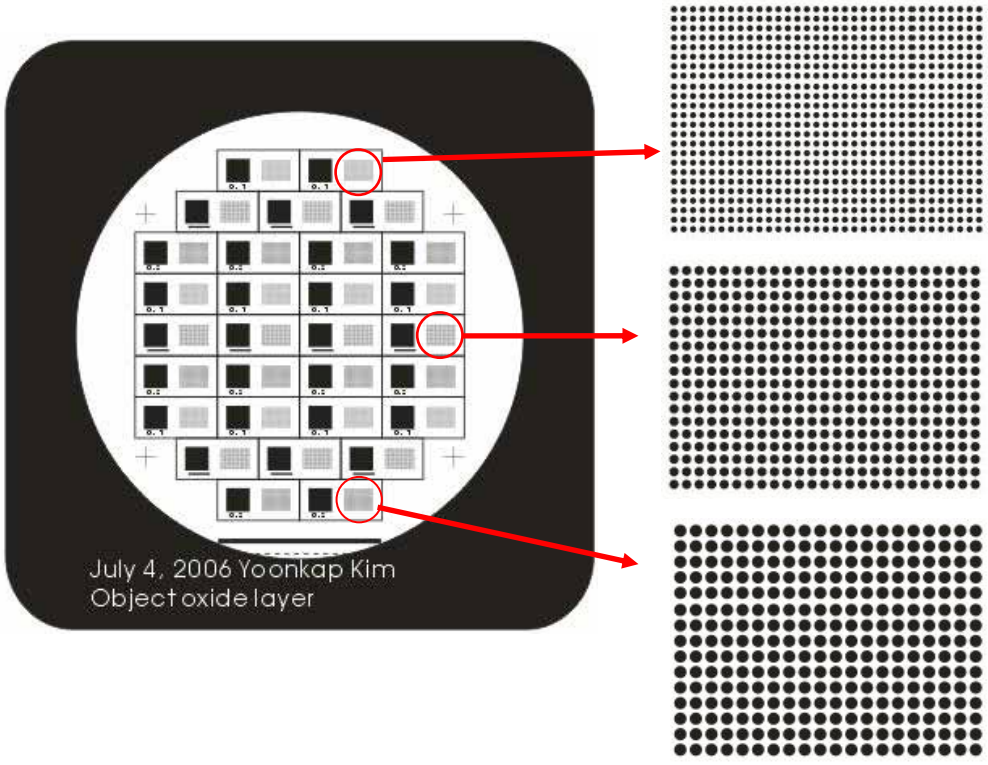

a) Mask for SiO_2 holes (100 μm, 150 μm, and 200 μm dots, and 4x4 mm square)

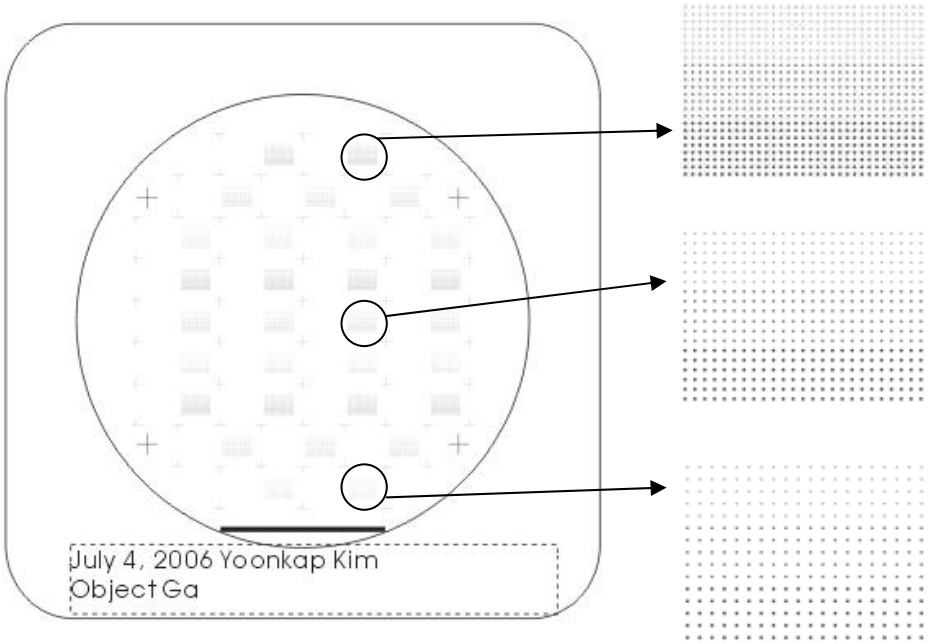

b) Mask for W (30 μm, 45 μm, and 60 μm dots)

Figure 2.1 Mask used for patterning

A patterned mask was used for the photolithography process. The mask was drawn in Corel Draw, and then printed on a transparent film in a screening process. The mask for W and SiO_2 is shown in figure 2.1. The mask consisted of thirty dies with various size dots. The size of each die was fourteen by seven mm. Each die pattern had 792, 450, and 300 dots ranging in diameter from 100 μm to 200 μm for SiO_2, and 264, 150, and 100 dots ranging in diameter from 30 μm to 60 μm for W. In addition, each pattern had a 4 x 4 mm square for electroplating and electrical performance testing. The polished surface of SiO_2 was coated with a thin AZ5214 photoresist film, and then the wafer was illuminated with UV light. The illuminated resist area became soluble. After patterning the photoresist, the oxidation layer was chemically etched in Buffered Oxide Etch (BOE) [39, 40]. A 10nm titanium / tungsten (Ti / W) layer for adhesion was DC

sputtered on the polished side of the wafer at 100W, and a 100nm W was then sputtered on the surface of Ti / W at 113W. After a photolithography process, the W and Ti / W layers were chemically etched in hydrogen peroxide (H_2O_2). The wafer was cleaned by 3 steps with acetone, isopropyl alcohol, and deionized (DI) water, and then diced into thirty test samples. The structures of the described fabrication process above are shown in figure 2.2.

(a) Boron doping: Evaporate B_3N_4 disk.

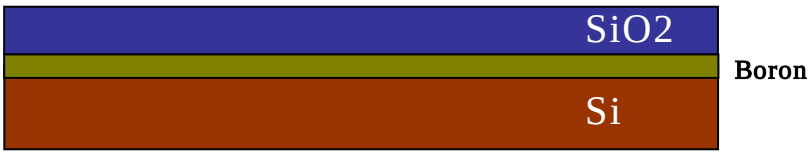

(b) Oxidation: Grow a thin (120nm-180nm) oxide layer on the B-Si substrate.

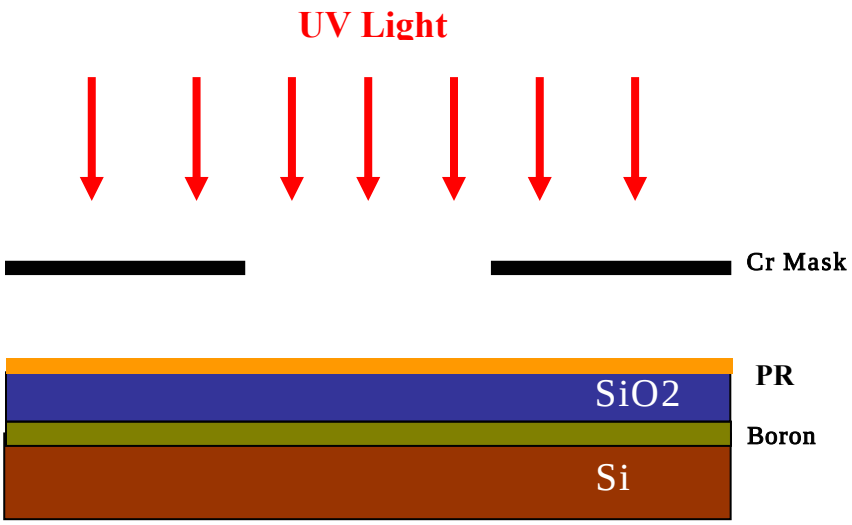

(c) Coat the surface of oxide with a thin photoresist film,

and then expose to UV light.

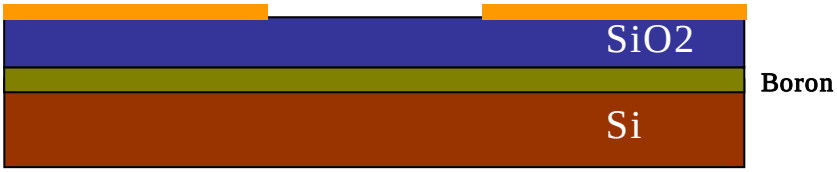

(d) Develop photoresist. This leaves only the regions of hardened resist.

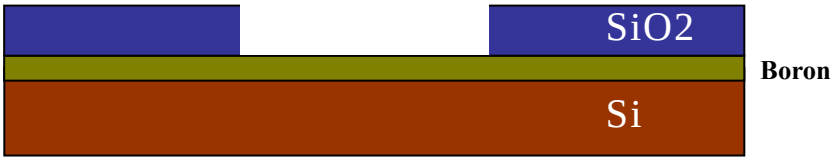

(e) Etch oxide by wet etching in BOE.

(f) Grow 10nm Ti/W adhesion layer and 100nmW on the surface by DC sputtering.

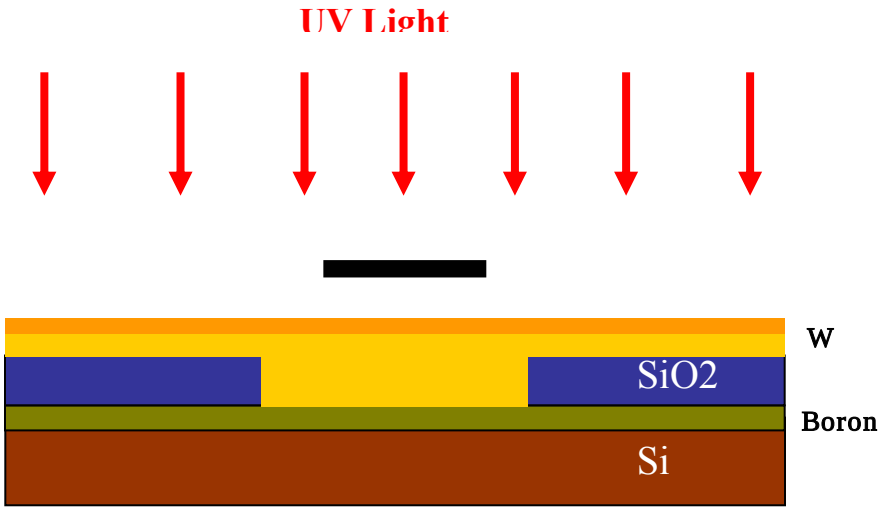

(g) Coat the surface of W with a thin photoresist film,

and then expose to UV light.

(h) Develop photoresist.

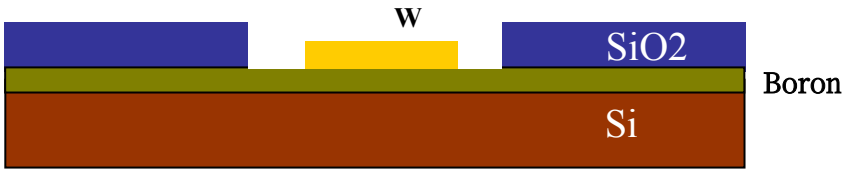

(i) Etch W by wet etching in H_2O_2.

Figure 2.2 Structure of fabrication process.

2.2 ELECTROPLATING PROCESSES FOR GALLIUM AND TIN

An electroplating process was used to deposit both gallium and tin. The condition of the electroplating process was differently applied for each metal, and electroplating time was decided by Faraday's equation [41],

$$w = \frac{ItM}{nF} \tag{2.1}$$

where w is the weight (g), I is the current (A), t is the time (s), M is the atomic mass of the metal, n is the valence of the metal ion, and F is Faraday's constant (96,500 C).

2.2.1 Electroplating of Gallium

The electrolyte consisted of gallium chloride and 140 ml solution of deionized (DI) water and hydrochloric acid (HCl). The pH of the solution was 1.5-2.5. The pH was controlled by HCl, and measured by hydrion paper. The electrolyte was carried out in a glass beaker, and the concentration of gallium was 2.5*M*. The glass beaker was placed on the hot plate to control the temperature. The optimum conditions for best current efficiency were a cathode current density of 100A/dm^2, and a cathode potential between -0.6 to -0.7 V, and the temperature was 40˚-50˚C [42]. A platinum wire and fabricated specimen were provided in the glass beaker as anode metal and cathode respectively. The voltage was applied to the cathode and anode during the desired plating time, and then Ga^{3+} deposited on the cathode as Ga.

2.2.2 Electroplating of Tin

Sodium stannate (19 oz/gal) and sodium hydroxide (2 oz/gal) were used for the electrolyte of electroplating tin, and the solution was prepared by dissolving the sodium stannate and sodium hydroxide in deionized (DI) water. The electrolyte was held in the glass beaker which was placed on a hot plate, and heated up to 93˚-98.8˚C. In this case, a

steel rod and fabricated specimen were immersed in the glass beaker as anode and cathode material for the flow of current. For optimum plating condition, the current density was from 45 to 65 ampere square feet (asf), and voltage was 6 V [43]. The voltage was applied during the desired plating time for each specimen.

2.3 CONTACT ANGLE MEASUREMENT

A test specimen with a micro-droplet was mounted to measure contact angle. A Metlab Epoxy Mounting system was used for mounting gallium sample because the mounting system had low curing temperature (room temperature). The epoxy was two component clear casting resin, so the mounted specimen was visible to the naked eye. After mounting sample, the part of mounting was cut with a diamond saw, and then the side of the sample was wet ground with sandpaper (120, 600, and 1200) to see the cross-section of the droplets. The droplets were illuminated with a fiber optic and images were captured by the microscope lens (M plan Apo series, Mitutoyo). The contact angle of the images was analyzed by using Scion Image (Scion Image Beta 4.03) [44]. Figure 2.3 shows the process to measure contact angle.

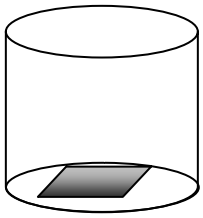

(a) Mounting sample.

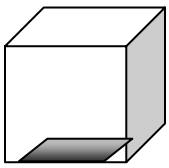

(b) After cutting the part of the sample, grinding the cross-section of the sample by sandpapers.

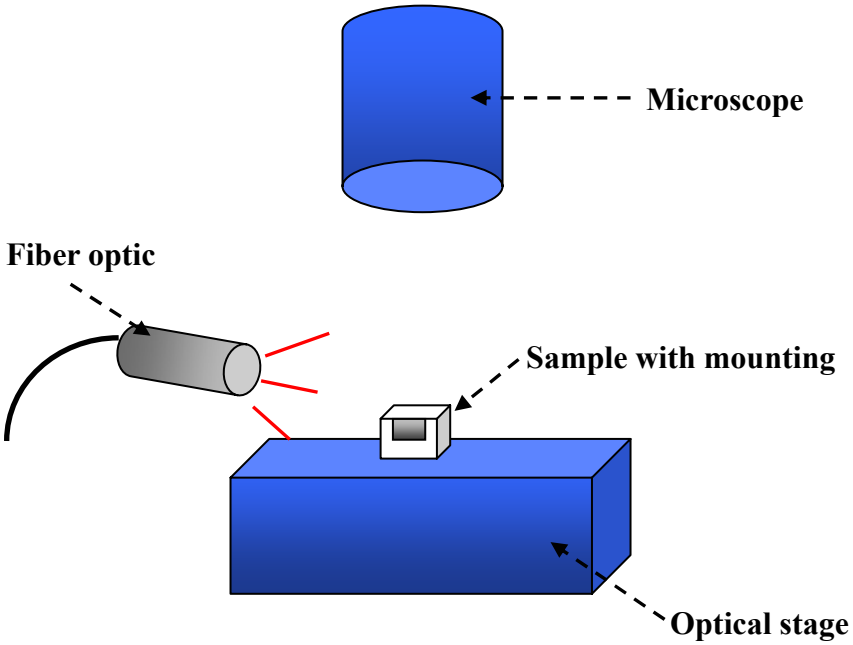

(c) Capturing and measuring the contact angle of the sample.

Figure 2.3 Schematic of the process of measuring contact angle.

2.4 ELECTRICAL PERFORMANCE

The electrical performance process was determined to evaluate the electrical properties of the micro-droplets for use as an electrical switch. To obtain the electrical performance, a special experimental setup was built. Figure 2.4 shows a simple schematic of the electrical performance experiment.

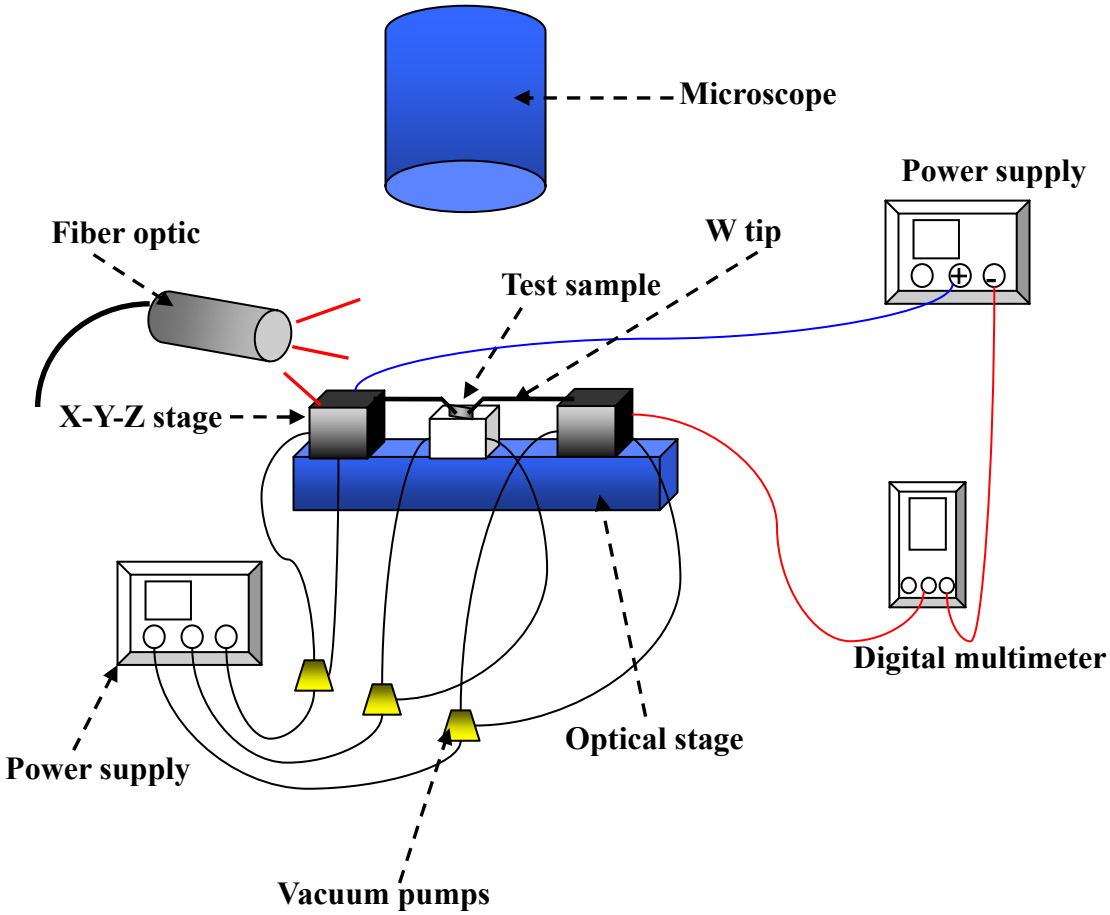

Figure 2.4 Simple schematic of the electrical performance experiment

The test sample with micro-droplets was placed on the bottom substrate, which

was connected with a vacuum pump, and fixed to the substrate by vacuum. To apply voltage to the test sample, two tungsten (W) tips were used to contact the micro-droplet for negative charge and etched B-Si surface (4 x 4 mm square) for positive charge. The W tips were mounted on micro actuators which can be controlled in the X, Y, and Z axes, and were connected with vacuum pumps and power supply. The W tip was controlled to contact on the surface of the micro-droplet through the microscope. After the each W tip was contacted to the micro-droplet and B-Si surface, voltage was applied by power supply. At that time, the current was measured by a Fluke 189 digital multimeter to produce current-voltage curves.

2.5 THERMAL REFLOW AND MICRO VICKERS HARDNESS TEST

2.5.1 Thermal Reflow

A thermal reflow process was used to observe the effect of temperature and reflow time on the structure of the micro-droplets. The thermal reflow test was carried out in a hot furnace. The temperature of the furnace was set by the desired temperature. When the temperature reached to the desired temperature, the test samples were put in the hot furnace. After the reflow time reached the setting time, and the temperature cooled down, the samples were taken out from the hot furnace. The surface of the test samples was captured and observed with a scanning electron microscope (SEM). Figure 2.5 schematically shows the thermal reflow process. All reflow was carried out in an ambient environment.

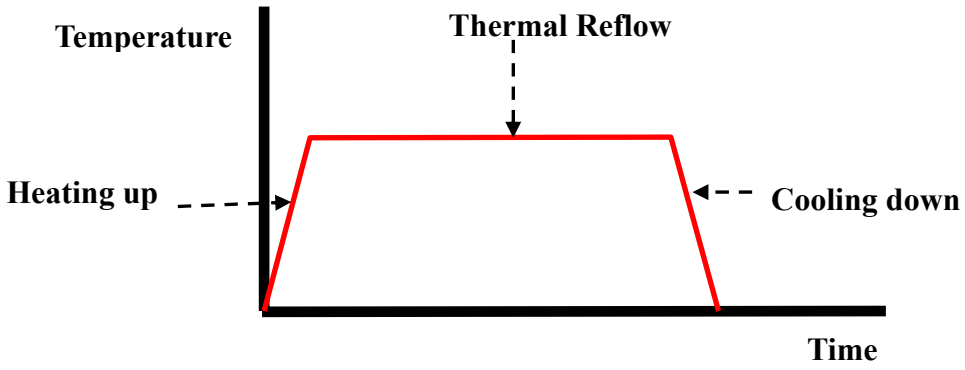

Figure 2.5 Chart of thermal reflow process

2.5.2 MICRO VICKERS HARDNESS TEST

The hardness of the micro-droplets was measured using a micro Vickers hardness test. A Leco M-400A micro hardness tester was used as measuring apparatus. The test specimen was mounted by Metlab Epoxy Mounting system, and then it was prepared as discussed in chapter 2.3. After the micro hardness tester was calibrated by using a calibrating specimen, the load was set up to low (10g) for gallium droplets. The prepared sample was mounted on the micro hardness tester, and the diamond tip of the tester was pressed into the surface of the droplet. After the magnification of the lens was adjusted to 100, the hardness of droplet was determined by measuring the residual impression. The surface of the droplet was observed through SEM.

CHAPTER 3

RESULT AND DISCUSSION

3.1 ELECTROPLATING TIN AND GALLIUM

Figure 3.1 shows the results of a 13 second tin (Sn) deposition on the 10 nm Ti / W and 100nm W layer using the mask shown in figure 2.1 with electroplating process. The electroplated tin was deposited on the desired spots. Figure 3.2 also shows the results of electroplating Gallium (Ga) droplets on the 10 nm Ti / W and 100nm W layer using the same mask for Sn for 78 sec. All Ga droplets were deposited on the desired spots.

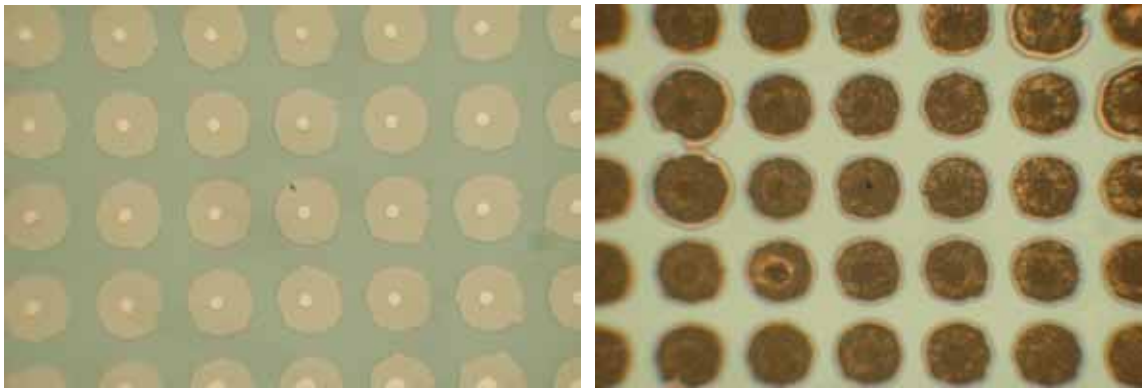

(a) Before deposition (b) After deposition

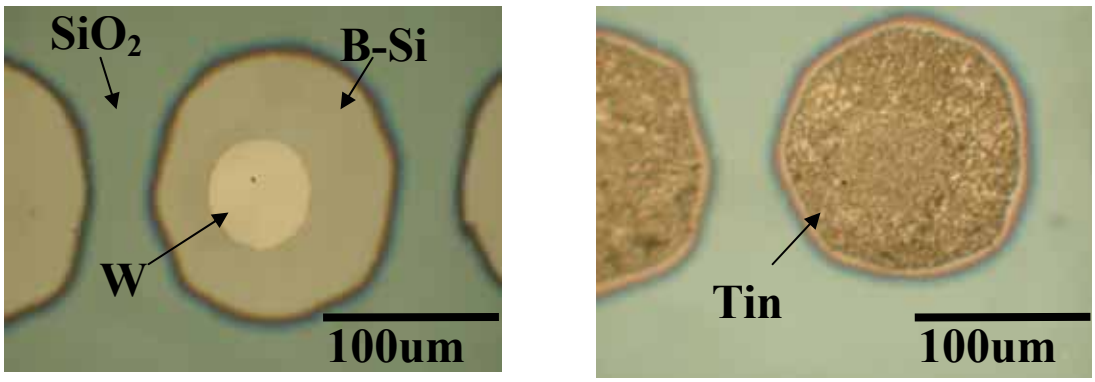

(c) Before deposition image (High Mag.) (d) After deposition image (High Mag.)

Figure 3.1 Portion of electroplated tin array for 13 sec.

Mask: 450 of 150 μm SiO2 hole and 60 μm W dot

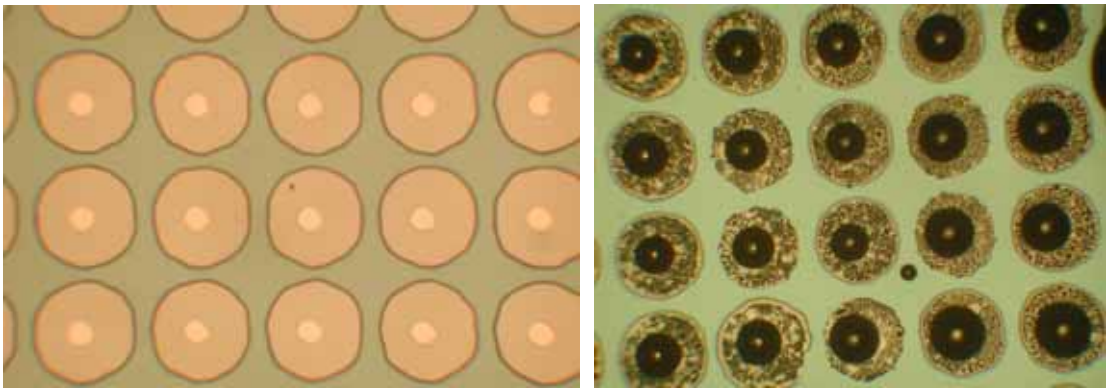

(a) Before deposition (b) After deposition

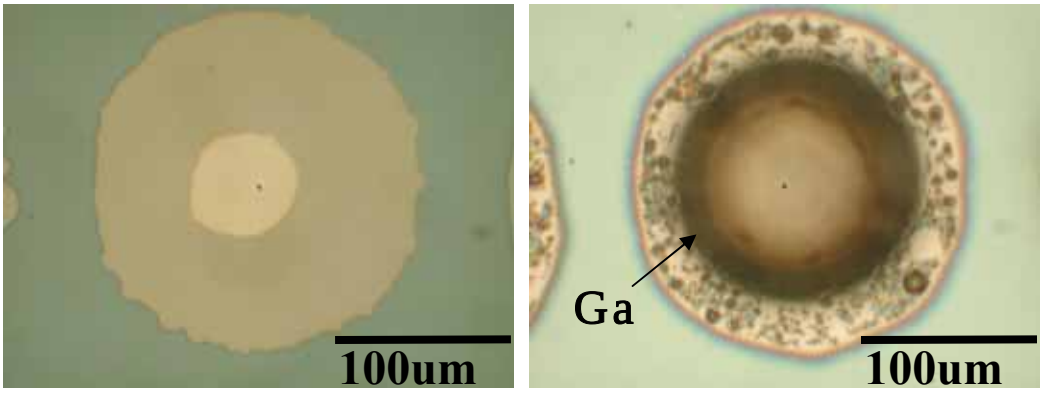

(c) Before deposition image (High Mag.) (d) After deposition image (High Mag.)

Figure 3.2 Portion of Ga micro-droplets.

Mask: 300 of 200 μm SiO2 hole and 60 μm W dot

Deposition time: 78 sec

3.2 THERMAL REFLOW EFFECTS

3.2.1 The Effect of Tin (Sn) by Tungsten (W) Spot and Silicon Hole Size after Thermal Reflow

Scanning Electron Microscopy (SEM) was applied to observe the surface of the samples before and after thermal reflow. Figure 3.3 shows SEM images of tin (Sn) deposition on the tungsten (W) dot to investigate the effect by W dot size relative to the exposed Silicon after thermal reflow. The thermal reflow temperature was 300 ˚C in an effort to melt the Sn.

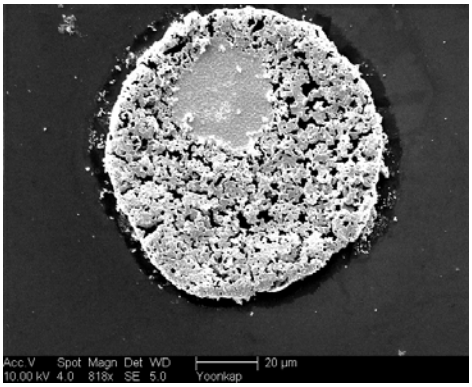

(a) Before thermal reflow (Sn on 30 µm W)

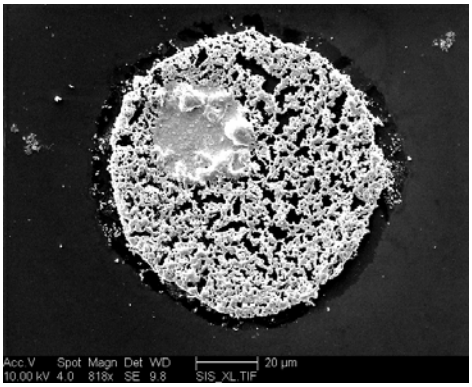

(b) After thermal reflow (Sn on 30 µm W)

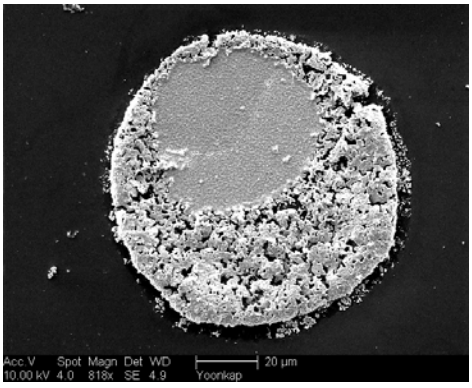

(c) Before thermal reflow (Sn on 45 µm W)

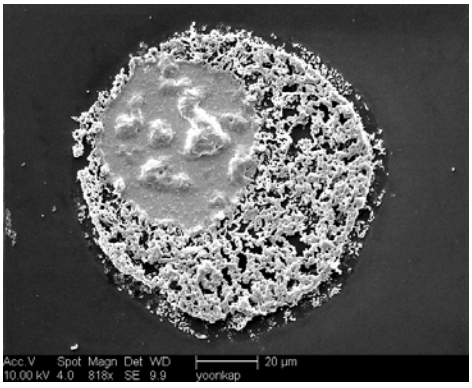

(d) After thermal reflow (Sn on 45 µm W)

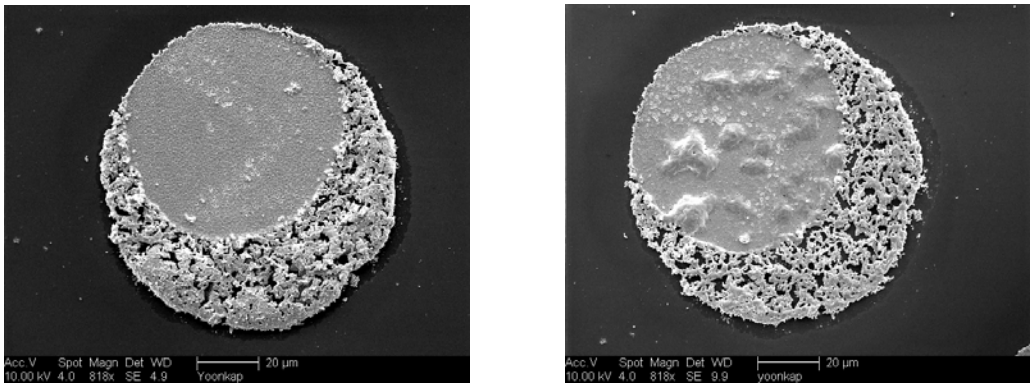

(e) Before thermal reflow (Sn on 60 µm W) (f) After thermal reflow (Sn on 60 µm W)

Figure 3.3 SEM images of Sn deposition on W dots (30-60 µm) in 0.1mm SiO_2 holes after thermal reflow.

Thermal reflow temperature: 300°C.

Thermal reflow time: 20 min.

It was observed that a small amount of Sn moved into the W spots after thermal reflow, and the quantity of Sn on each W spot was almost the same through figure 3.3. This movement of Sn was also observed by a change in the porosity of Sn. After thermal reflow, the sizes of the pores increased, as seen in figure 3.3, because a small amount of Sn was transferred from outside of the W spot to the inside in contact with the W. It can be concluded that Sn does react with W above its melting temperature, but it is not significantly affected by W spot size. Figure 3.4 shows SEM images of Sn deposition in different SiO_2 hole sizes after thermal reflow. As seen in figure 3.4 (a), (c), and (e), the small quantity of Sn was moved from entire area of the SiO_2 hole to the W dot.

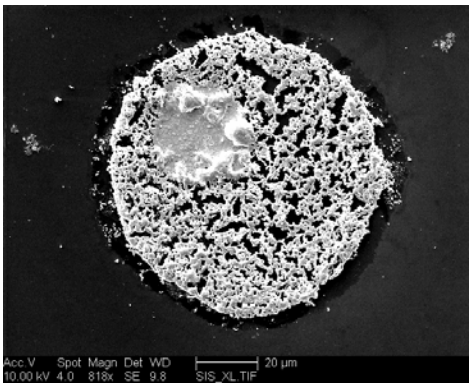

(a) Sn on 30 µm W in 0.1 mm SiO_2 hole

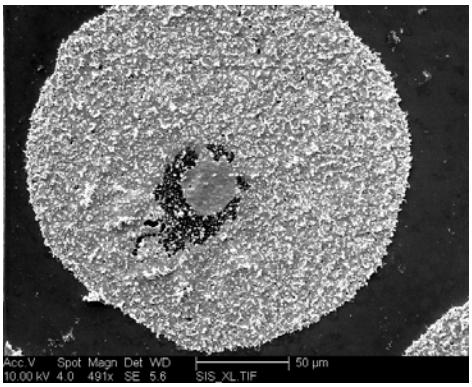

(b) Sn on 30 µm W in 0.2 mm SiO_2 hole

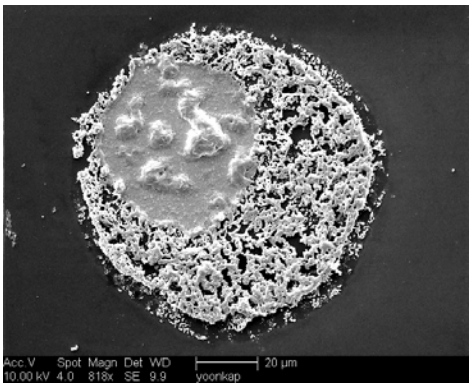

(c) Sn on 45 µm W in 0.1 mm SiO_2 hole

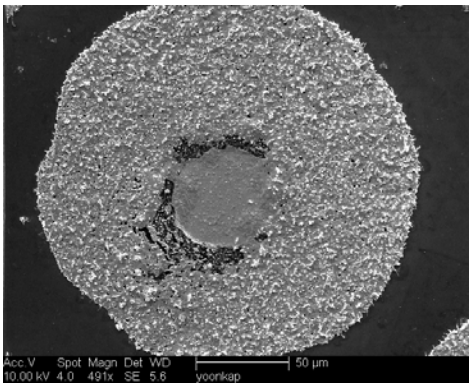

(d) Sn on 45 µm W in 0.2 mm SiO_2 hole

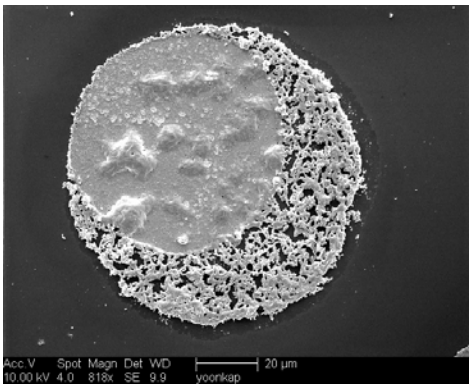

(e) Sn on 60 µm W in 0.1 mm SiO_2 hole

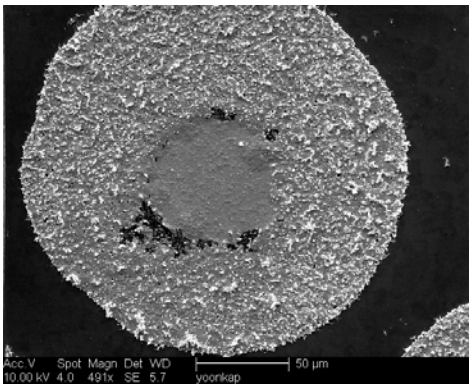

(f) Sn on 30 µm W in 0.2 mm SiO_2 hole

Figure 3.4 SEM images of Sn deposition on W dots (30-60 µm)

in 0.1 mm and 0.2 mm SiO_2 holes after thermal reflow.

Thermal reflow temperature: 300˚C, Thermal reflow time: 20 min.

In the 0.2 mm SiO_2 hole case, Sn was just transferred from the area close to the W dot to the W area as seen in figure 3.4 (b), (d), and (f). Therefore, the quantity of Sn moved onto W spots in the 0.1 mm SiO_2 holes was greater than for the 0.2 mm SiO_2 holes. It means that the amount of reacted Sn with W is affected by SiO_2 hole sizes, and the distance the Sn must move to reach the W surface.

3.2.2 The Effect of Thermal Reflow Time on Tin (Sn) electrodes

Figure 3.5 shows SEM images of the change of Sn in a 0.1 mm SiO_2 hole by thermal reflow time. As thermal reflow time increases, the amount of shifted Sn to W dot was increased. After reflowing for 2 hours, Sn covered the W spot as shown in figure 3.5 (d), and after reflow for 4 hours, it was observed that the deposited Sn shrunk to W area, and then the quantity of Sn in outside of SiO_2 hole was decreased through figure 3.5 (e). This indicates that more Sn moves into W dot as the thermal reflow time increase, so the reflow time is an important factor for movement of melted Sn. However, in no case were we able to completely clear the Si substrate of all Sn.

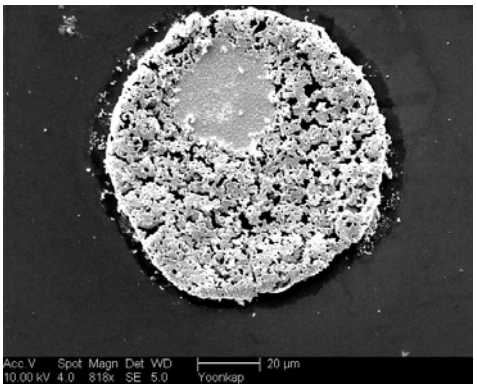

(a) Before thermal reflow

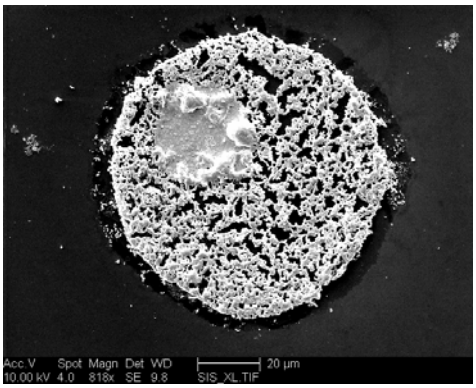

(b) Thermal reflow for 20 min.

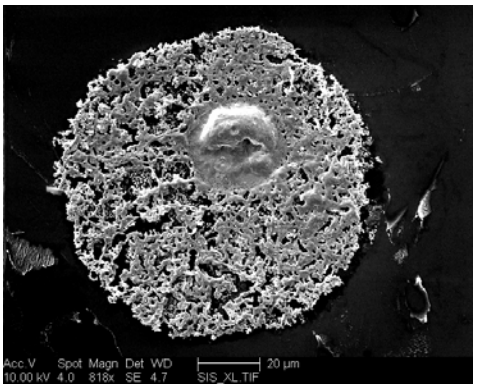

(c) Thermal reflow for 1 hour

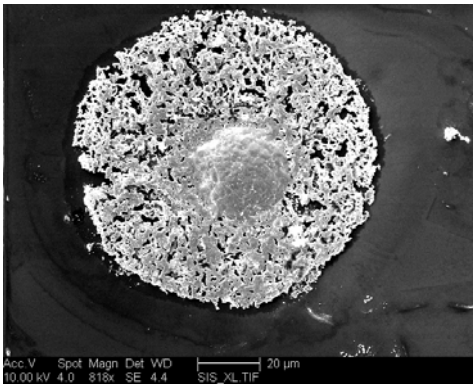

(d) Thermal reflow for 2 hour

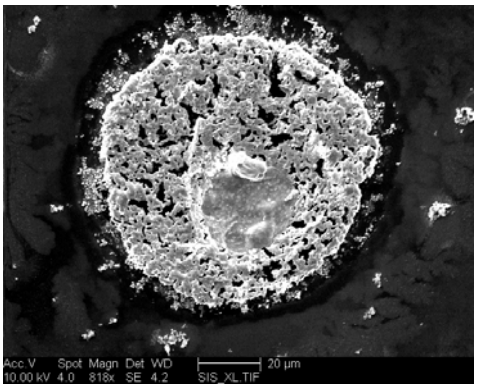

(e) Thermal reflow for 4 hour

Figure 3.5 SEM images of the change of Sn deposition on 30 µm W dots in 0.1 mm SiO_2 holes by thermal reflow time.

Thermal reflow temperature: 300˚C.

3.2.3 The Effect Tungsten (W) Spot and Silicon Hole Size after Thermal Reflow for Gallium

Figure 3.6 shows the SEM images of gallium (Ga) droplets on various W dot sizes (30 µm - 60 µm) in 0.2 mm SiO_2 holes after thermal reflow at 100˚C for 10 min. The SEM images were tilted 45 degree to observe the change of the surface shape of Ga droplets. The Ga deposition had much less unwanted deposition on the Si substrate.

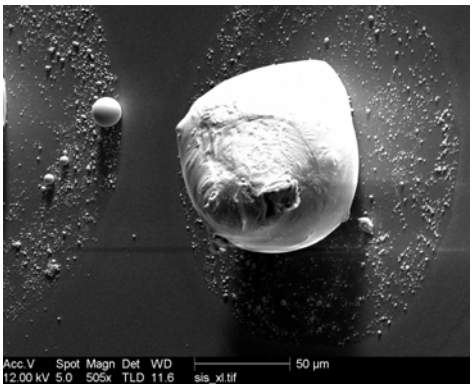

(a) Before thermal reflow
(Ga on 30 µm W)

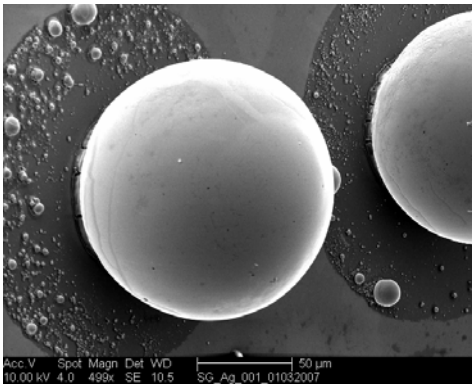

(b) After thermal reflow
(Ga on 30 µm W)

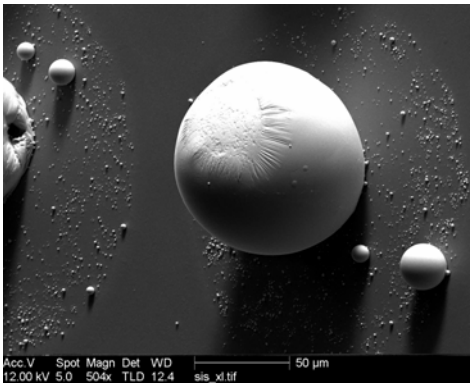

(c) Before thermal reflow
(Ga on 45 µm W)

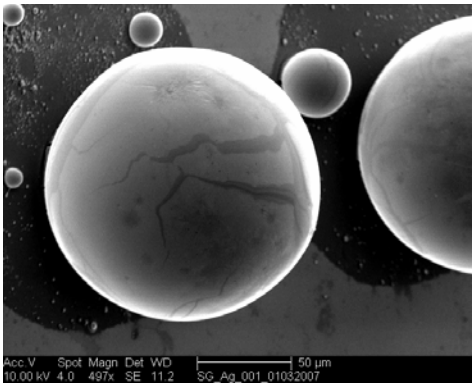

(d) After thermal reflow
(Ga on 45 µm W)

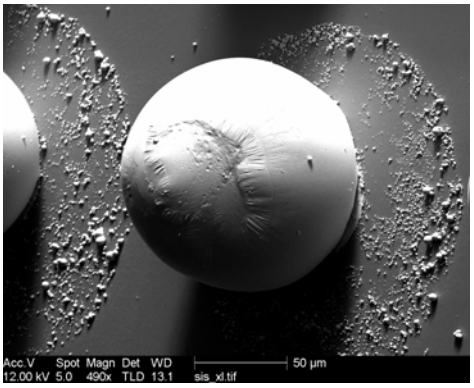

(e) Before thermal reflow
(Ga on 60 µm W)

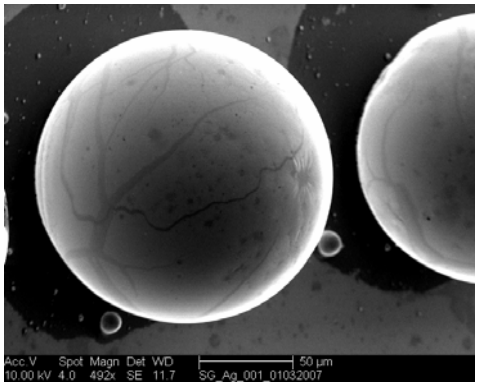

(f) After thermal reflow
(Ga on 60 µm W)

Figure 3.6 SEM images of gallium (Ga) droplet on various W dot sizes

(30 µm - 60 µm) in 0.2 mm SiO_2 holes after thermal reflow at 100°C for 10 min.

Before thermal reflow, it was observed that the surfaces of Ga droplets were rough as shown in figure 3.6 (a), (c), and (e), but after thermal reflow, the surfaces were smoothly, and the droplet became more spherical in shape as seen in figure 3.6 (b), (d), and (f). The Ga droplets were deposited on W dots, and the deposited quantity showed minute difference as W dot sizes. It can be concluded that the surface shape of Ga droplet is influenced by thermal reflow, but the quantity of Ga droplets is not seriously affected by W dot size. This property of Ga can be used to heal the worn surface of droplets in the MEMS switches.

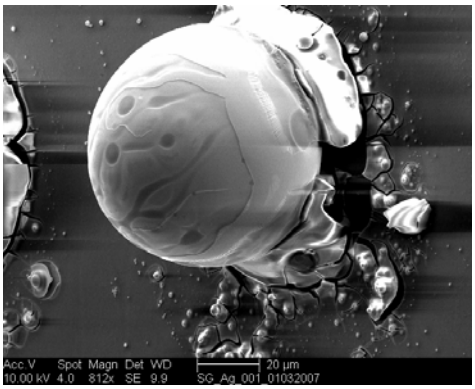

(a) Ga droplet in 0.1 mm SiO_2 hole

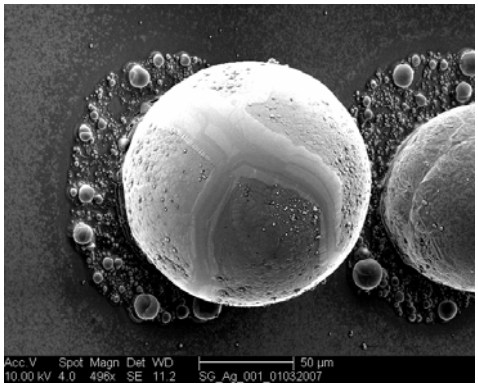

(b) Ga droplet in 0.15 mm SiO_2 hole

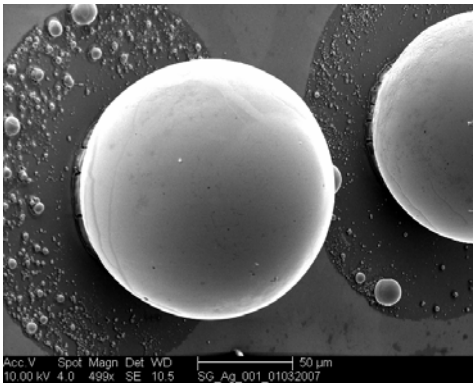

(c) Ga droplet in 0.2 mm SiO_2 hole

Figure 3.7 SEM images of gallium (Ga) droplet on 30 µm W dot in various SiO_2 hole sizes (0.1 mm – 0.2 mm) after thermal reflow at 100°C for 10 min.

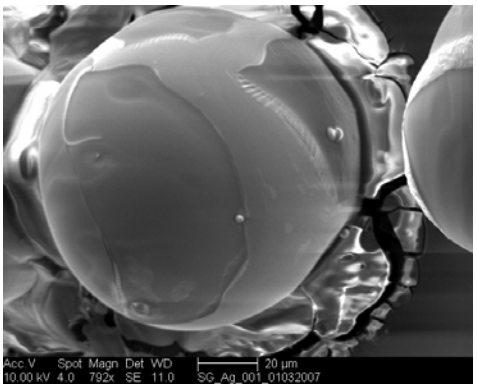

(a) Ga droplet in 0.1 mm SiO_2 hole

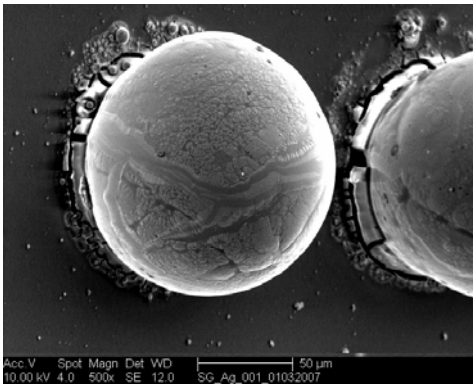

(b) Ga droplet in 0.15 mm SiO_2 hole

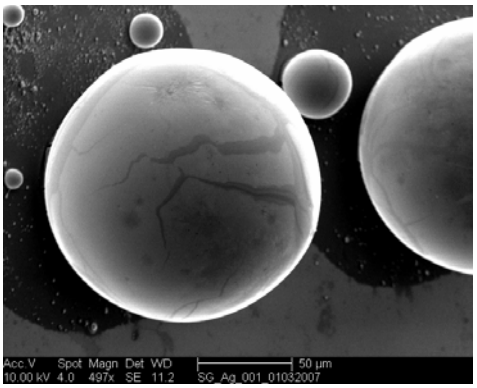

(c) Ga droplet in 0.2 mm SiO_2 hole

Figure 3.8 SEM images of gallium (Ga) droplet on 45 µm W dot in various SiO_2 hole sizes (0.1 mm – 0.2 mm) after thermal reflow at 100°C for 10 min.

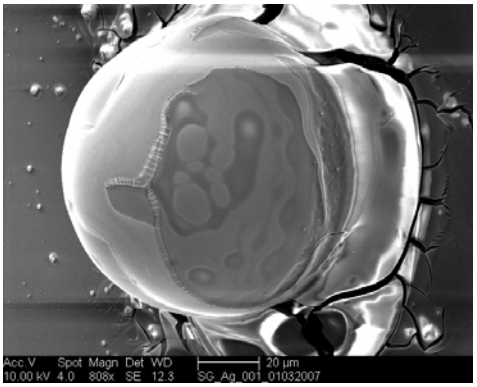

(a) Ga droplet in 0.1 mm SiO_2 hole

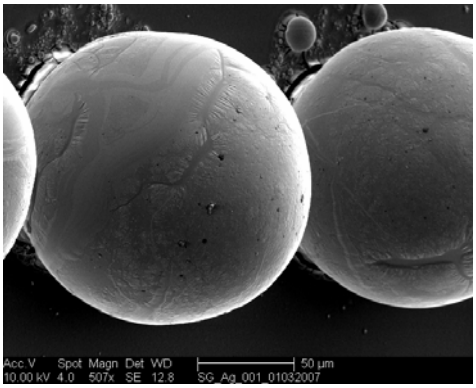

(b) Ga droplet in 0.15 mm SiO_2 hole

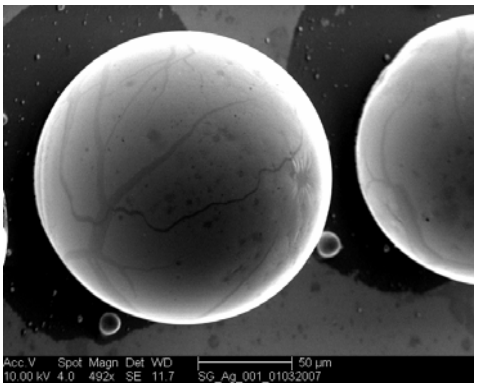

(c) Ga droplet in 0.2 mm SiO_2 hole

Figure 3.9 SEM images of gallium (Ga) droplet on 60 µm W dot in various SiO_2 hole sizes (0.1 mm – 0.2 mm) after thermal reflow at 100˚C for 10 min.

In particular, a region around the W spot was "cleared" of specious Ga deposition after reflow. Figure 3.7, 3.8, and 3.9 show the SEM images of Ga droplets in various SiO_2 hole size (0.1 mm- 0.2 mm) after thermal reflow at 100˚C for 10 min. In the figure 3.7, as increasing the SiO_2 hole size, the Ga droplet sizes were increased and the surface quality of Ga droplet was improved after thermal reflow. This situation was also observed in figure 3.8 and 3.9. It means that the surface state and size of Ga droplets is affected by the SiO_2 hole size, but it is not influenced by W dot size or rate of W to SiO_2 as discussed above. In addition, the condition of electroplated Ga droplets in the large SiO_2 hole size (0.2 mm) case was more uniform than in the small SiO_2 holes (0.1 mm).

3.2.4 The Effect of Thermal Reflow Time and Temperature on Ga droplets

The droplets in the MEMS switch may spread out during the operation of the switch. In this case, it would be desirable to have the spread droplets come back to their spherical original shape. To observe the reflow of Ga droplets, the Ga droplets were

incompletely deposited on W spots in the 0.2 mm SiO_2 holes by decreasing electroplating time. Figure 3.10 shows the SEM images of the changes of the Ga droplets by thermal reflow time at 100˚C. Small Ga droplets were placed on 60 μm W dot. As seen in figure 3.10, the small droplets did not reflow into the center of W dot, and combine with each other at increasing thermal reflow time. However, the change of the surface shape of Ga droplets was observed through figure 3.10 (b) and (c).

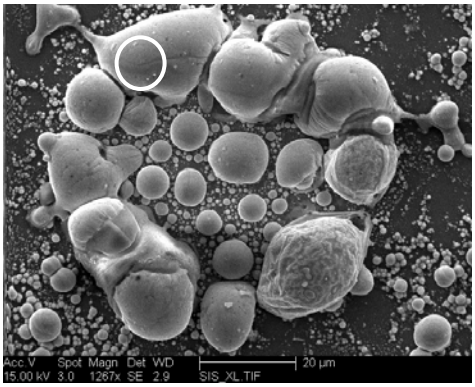

(a) Before thermal reflow

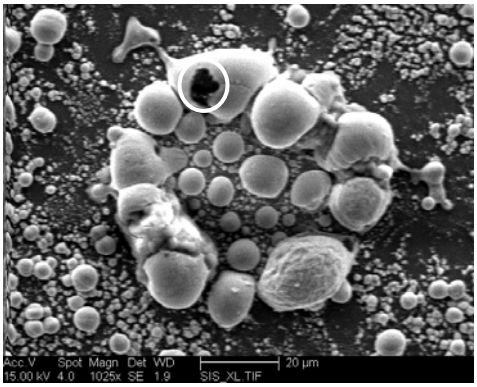

(b) Thermal reflow for 10 min.

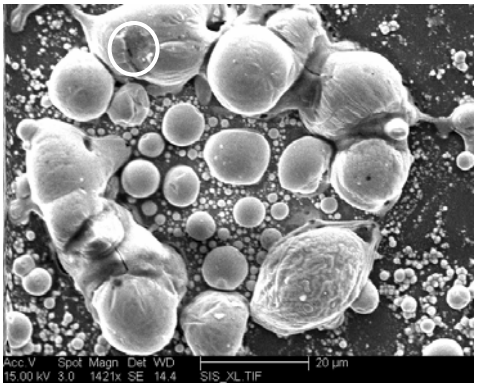

(c) Thermal reflow for 30 min.

Figure 3.10 SEM images of the change of the incompletely deposited Ga droplets by thermal reflow time.

W dot size: 60 μm.
SiO_2 hole size: 0.2 mm
Thermal reflow temperature: 100 ˚C

Figure 3.11 shows the SEM images of the change of the Ga droplets as increasing thermal reflow temperature. In this case, although temperature was increased until 300 ˚C, the small Ga droplets did not come back to inside of W dot, but the change of the droplet surface was observed in figure 3.11. Before thermal reflow, two droplets in the red circle were contacted as shown in figure 3.11 (a). As increasing the reflow temperature necking occurred, blurring the boundary between the two droplets as seen in figure 3.11 (b), and the boundary line disappeared at 250 ˚C and 300 ˚C as in figure 3.11 (d) and (e). It means that the two droplets were combined with each other.

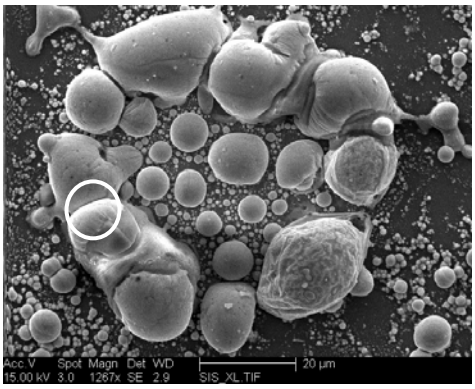

(a) Before thermal reflow

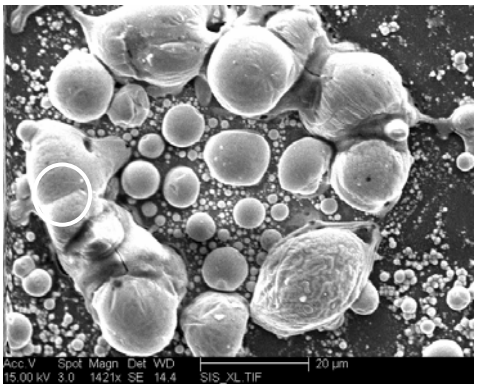

(b) After thermal reflow at 100 ˚C

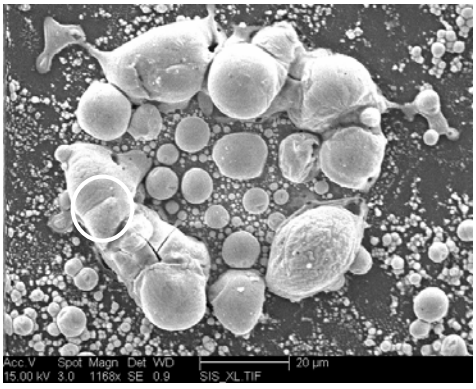

(c) After thermal reflow at 120 ˚C

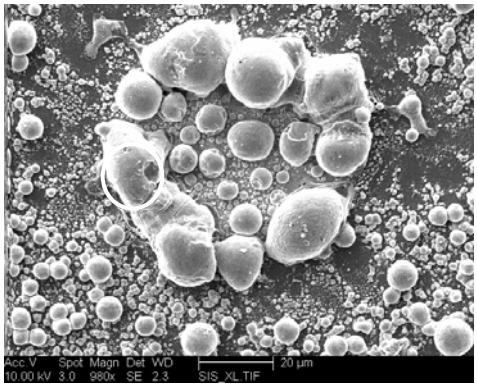

(d) After thermal reflow at 250 ˚C

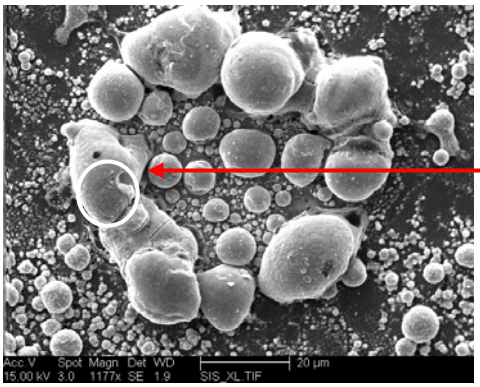

(e) After thermal reflow at 300 ˚C

Figure 3.11 SEM images of the change of the incompletely deposited Ga droplets as increasing thermal reflow temperature.

W dot size: 60 μm.
SiO_2 hole size: 0.2 mm
Thermal reflow time: 30 min.

Figure 3.12 shows the SEM images of the change of the incompletely deposited Ga droplets on W cross spots as increasing thermal reflow temperature. In this case, the shape of the W spot was changed from circle to cross, and the small Ga droplet surfaces were observed though figure 3.12.

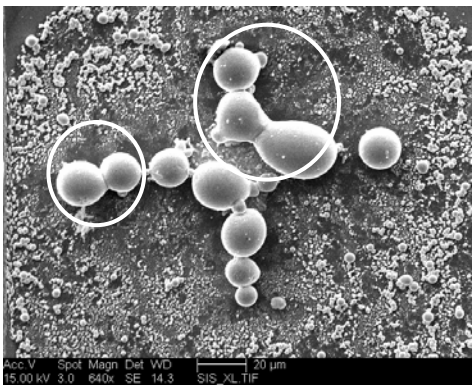

(a) Before thermal reflow

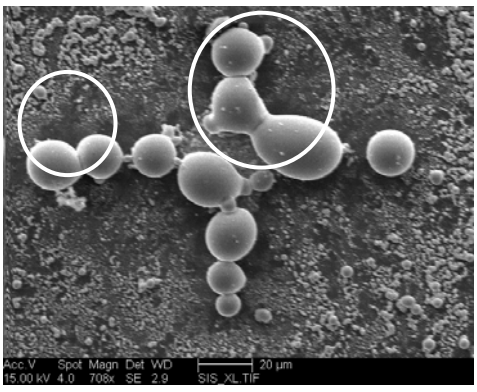

(b) After thermal reflow at 100 ˚C

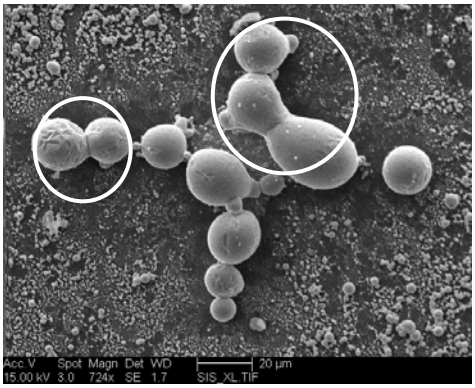

(c) After thermal reflow at 120 ˚C

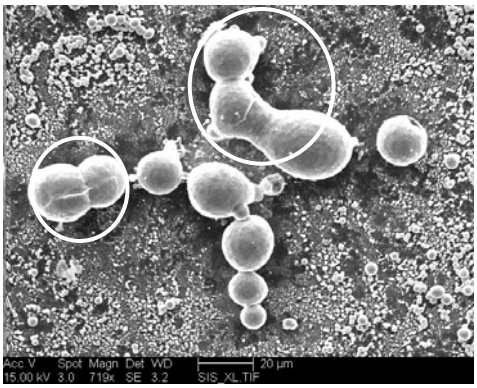

(d) After thermal reflow at 250 ˚C

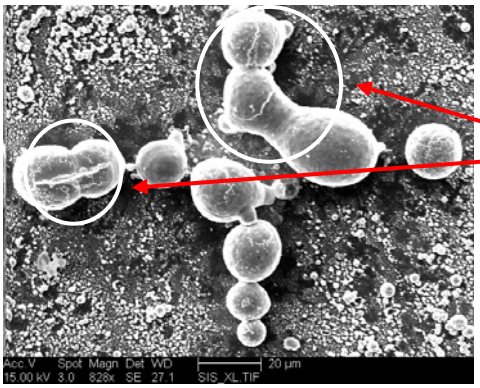

(e) After thermal reflow at 300 ˚C

Figure 3.12 SEM images of the change of the incompletely deposited Ga droplets on W cross spots as increasing thermal reflow temperature.

W cross spot size: 125 μm.
SiO_2 hole size: 0.2 mm
Thermal reflow time: 30 min.

In the figure 3.12 (a) and (b), there was no change of the Ga droplets until 100 ˚C, but the droplets in the circles started to combine after 120 ˚C, as seen in figure 3.12 (c), and especially the two droplets in the small circle were completely combined with each other at 300 ˚C, as shown in figure 3.12 (e). However, there was no reflowing Ga droplets to inside of W spot as increasing reflow temperature.

Although there were the change of the small Ga droplets surface and combining of the droplets, yet there was no reflow to inside of W dot as the expected result after thermal reflow.

3.3 CONTACT ANGLE OF GALLIUM (Ga) DROPLET ON TUNGSTEN (W) DOT

In the experiment, Ga droplets were deposited on 60 μm W dot in 0.2 mm SiO_2 hole. Figure 3.13 shows the cross-section of deposited Ga droplets to measure contact angle. Figure 3.14 shows the top view of Ga droplets on 60 μm W dot after wet grinding. The center cross-section of the droplets was used for accurate measurement of contact angle, and it was verified through figure 3.13.

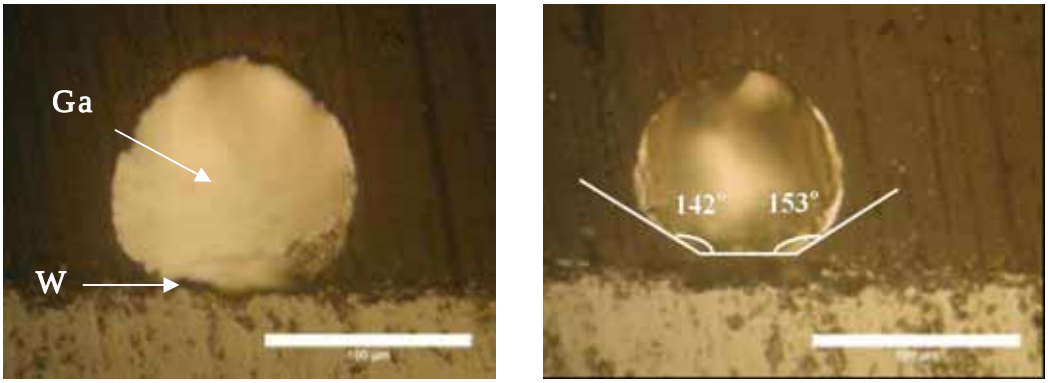

(a) Cross-section of Ga droplet (b) Average contact angle: 148˚

Figure 3.13 The cross-section of Ga droplets on 60 μm W dot by wet grinding.

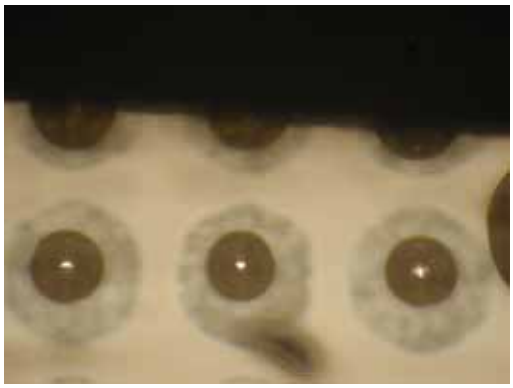

Portion of Ga droplets array

Figure 3.14 The top view of Ga droplets on 60 μm W dot after wet grinding.

If deviation from tangential lines in the image were more than ± 5˚, the uncertainty on the contact angle was ± 5˚. As seen in the figure 3.13 (b), the average contact angle of the Ga droplets were approximately 148˚ ± 5˚. It indicates that the Ga droplets were non-wetting condition because the contact angle was higher than 90˚, but in this case, the electroplated Ga droplet size was bigger than W dot size. Therefore, smaller Ga droplets were deposited on 45 μm W dots in the 0.2 mm SiO_2 hole, and the electroplating time for Ga was decreased to reduce the droplet size.

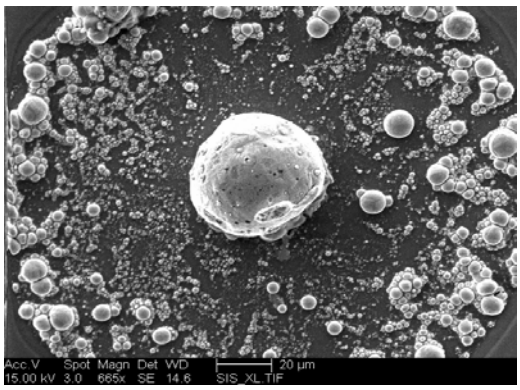

(a) SEM image before mounting and wet grinding

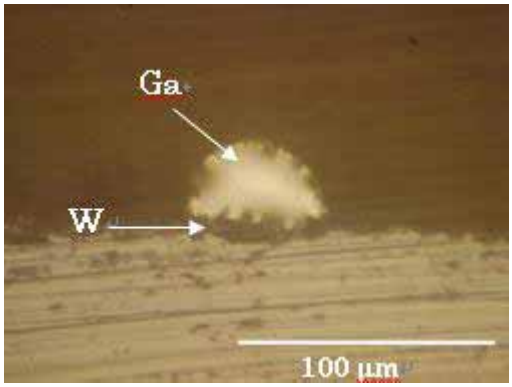

(b) Cross-section of the Ga droplet

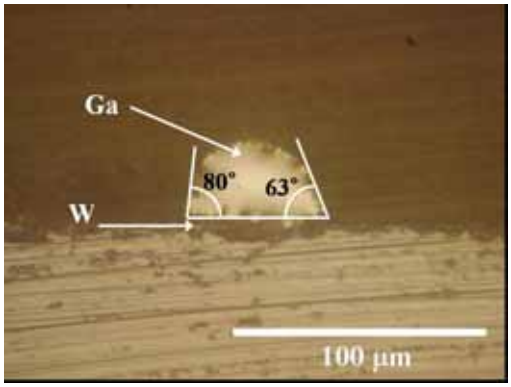

(c) Average contact angle: 72˚

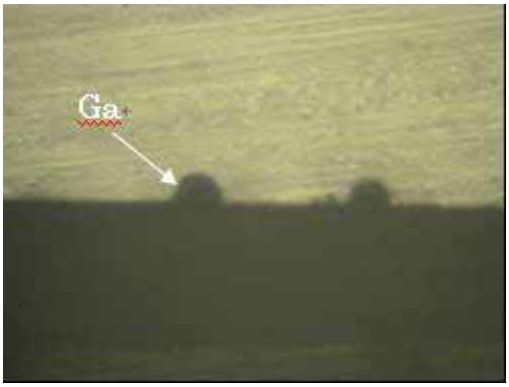

(d) Cross-section of the Ga droplet

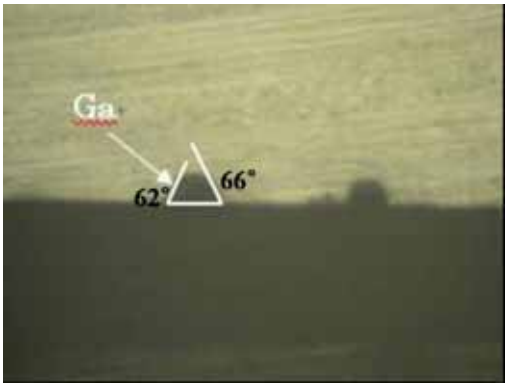

(e) Average contact angle: 64˚

Figure 3.15 SEM image and cross-section of the reduced Ga droplets on 45 μm W dot.

Figure 3.15 shows the SEM image and cross-section of reduced Ga droplet on 45 μm W dot in 0.2 mm SiO_2 hole by decreased electroplating time. As shown in figure 3.15 (c) and (e), the average contact angles of deposited Ga droplets were 72˚ ± 5˚and 64˚ ± 5˚ which are typical value for partial wetting condition of Ga droplets. It means that the adhesive force of W and Ga is greater than the cohesive force of Ga droplet surface. Therefore, it can be concluded that the Ga droplet had good adhesion with the W dots. However, deposition beyond the amount needed to cover the W target leads to the lack of wetting when Ga contacts the SiO_2 surface.

3.4 ELECTRICAL PERFORMANCE OF THE GALLIUM (Ga)

The electrical properties of Ga droplets were observed by current-voltage scans. Figure 3.16 shows a typical voltage-current curve of the Ga droplets on W dots. In this figure 3.16, the slope value represents the total conductance (31.457 mA/V). The total conductance can be converted to resistance by Ohm's law (V = I R). The total resistance value was 31.79Ω. Uncertainty for the voltage measurement of 2.8V across the Ga droplet is ± 0.07V, and uncertainty for the typical current of 0.83A is ± 0.125A. These uncertainty values were calculated from the manual of the Fluke 189 digital multimeter The root sum of squares method (RSS) was used to find the uncertainty on the resistance. The RSS method is expressed as equation 3.1

$$w_R = \left[\sum_{i=1}^{n} \left(\frac{\partial F}{\partial x_i} w_{xi} \right)^2 \right]^{1/2} \tag{3.1}$$

where the uncertainty w_R where the function of interest F is differentiated with respect to parameters x_i each having an uncertainty w_{xi} [45]. The uncertainty on the resistance was calculated by using equation 3.1 with the typical value of the voltage and current, so the uncertainty on the total resistance was 31.79Ω ± 0.5Ω. The ohmic heating was calculated from Joule's law. The Joule's law is represented as equation 3.2

$$\mathrm{Q} = I^2 R t \tag{3.2}$$

where I is flowing current, R is resistance, and t is following time. The flowing current was 0.83A and the resistance was 31.79 Ω for 2 seconds. The ohmic heating was calculated to 43.8J as the flowing current, resistance, and time substituted to equation 3.2. The heating energy is also expressed as

$$\mathrm{Q} = mC\Delta T \tag{3.3}$$

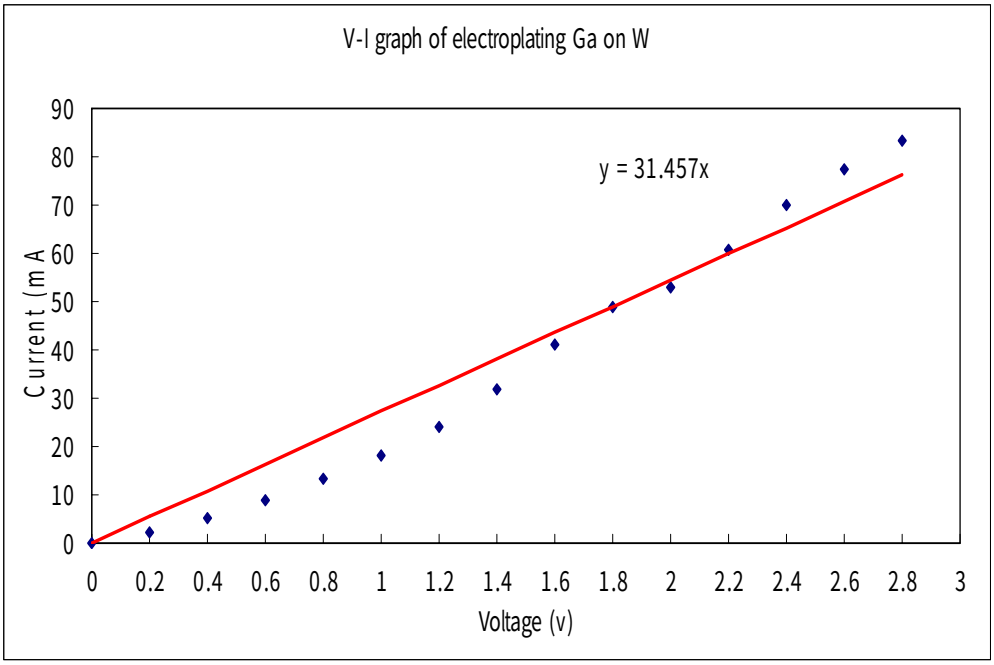

Figure 3.16 Voltage-current plot of deposited Ga droplets on W dots

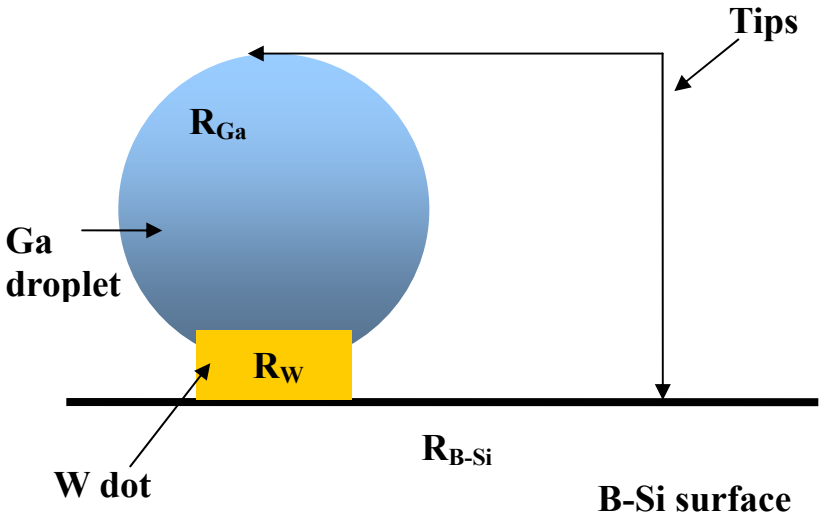

Figure 3.17 Simple schematic of component of the total resistance.

where m is mass of substance, C is the specific heat capacity, and ΔT is the temperature differential($T-T_0$). The specific heat capacity and mass of the Ga are 371J/kgK and 0.069kg respectively. These values and the ohmic heating energy 43.8J were substituted into equation 3.3 to calculate the temperature. The ΔT was calculated to 1.711K. The electronic test was performed at roomtemperature (300K), so the ohmic heating temperature was calculated to 301.7K. Therefore, we will ignore the heating due to $\Delta T <$ 1%. The total resistance consists of the resistances of Ga, W, and Boron (B)-doped Si. Figure 3.17 shows simple schematic of component of the total resistance. The resistance is expressed as equation 3.4

$$R = \rho \frac{l}{A}, \tag{3.4}$$

where l is the length of the conductor, A is the cross-sectional area of the conductor, ρ is the electrical resistivity (Ω cm) [24]. The total resistance (R_{total}) is represented as

$$R_{total} = \rho_{B\text{-}Si}\frac{l_{B-Si}}{A_{B-Si}} + \rho_W \frac{l_W}{A_W} + \rho_{Ga}\frac{l_{Ga}}{A_{Ga}} \tag{3.5}$$

In the experiment, the resistivity values of B-Si and W were 10^{-3} Ω cm and 5 x 10^{-6} Ω cm respectively [21, 46], so the resistances of B-Si and W ($R_{B\text{-}Si}$ and R_W) were calculated to 31.78 Ω and 3.458 x 10^{-6} Ω respectively. The resistivity value of Ga droplets (ρ_{Ga}) was calculated from the equation 3.5 by using the value of $R_{B\text{-}Si}$ and R_W. The ρ_{Ga} value was equal to 1.128 x 10^{-5} Ω cm, and the uncertainty on the ρ_{Ga} was 1.128 x $10^{-5} \pm 0.6$ x 10^{-5} Ω cm. The ρ_{Ga} value was very close to theoretical resistivity value of Ga (1 x 10^{-5} Ω cm). It implies that the Ga droplet has high conductivity for MEMS switches, and matches what would be expected for this material. The current device resistance is dominated by the boron doped silicon, and in a revised device would need

to be lowered.

3.5 MICRO VICKERS HARDNESS OF THE GALLIUM (Ga) DROPLET

Figure 3.18 SEM images of Ga droplet after micro Vickers hardness test. It was observed that the intensity of Ga droplet was soft as seen in figure 3.17 because the shape of a perfect indentation made with a perfect diamond-pyramid indenter is a square. However, the indentation of Ga droplet was not a perfect square, and the folds in the surface of Ga droplet were observed around the hardness test impression in the figure 3.17 (b). The folds around an indentation are usually found in soft surface. The Vickers hardness of Ga droplet is shown in table 3.1. Table 3.1 exhibits the Vickers hardness of the droplets as the test load. In table 3.1, the average of Vickers hardness value of the Ga droplets was 17.2 HV. The maximum applied stress can be calculated with the Vickers hardness value of the Ga droplets and mean pressure (P_m).

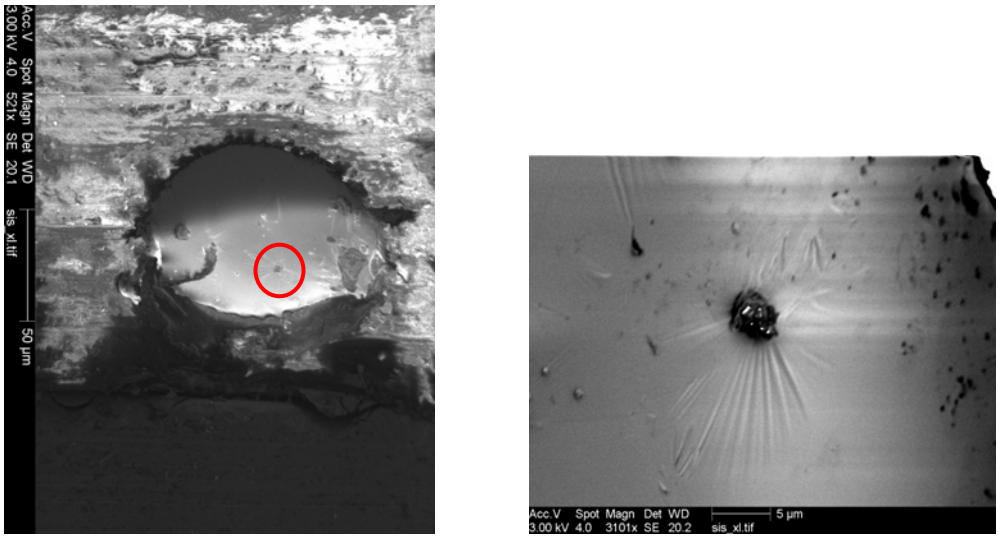

(a) Ga droplet after micro Vickers hardness test

(b) Enlarged image of the micro Vickers hardness test impression

Figure 3.18 SEM images of Ga droplet after micro Vickers hardness test.

Load	HV
1. low (10g)	**18.1**
2. low (10g)	**9.71**
3. low (25g)	**18**
4. low (25g)	**22.1**
5. low (25g)	**19**
6. high (50g)	**16.3**
Average	**17.2**

Table 3.1 Vickers hardness of the Ga droplets as the test load

The mean pressure is expressed as equation 3.6 and 3.7

$$P_m = 10.54\ HV \tag{3.6}$$

$$P_m = 3\sigma_y \tag{3.7}$$

where σ_y is yield strength and HV is Vickers hardness [47]. The mean pressure was calculated as the Vickers hardness of the Ga droplet substitutes into the equation 3.6. Finally, the yield stress is calculated to 60 MPa from equation 3.7, so we can suggest the maximum applied stress that can be applied to a Ga droplet in a MEMS device is 60 MPa. The maximum applied load is represented as equation 3.8

$$P = \frac{r^2(\pi\sigma_y)^3}{0.227E^2} \tag{3.8}$$

where r is radius of droplet and E is elastic modulus [48]. The elastic modulus of the Ga was 9.81GPa and the radius of the Ga droplet, which was deposited on the 60μmW dot, was 50μm. The uncertainty on the radius of the Ga droplet is ± 5 μm, so the

maximum load was calculated to 77 ± 15 μN as the elastic modulus and the radius of the Ga, and the maximum applied stress substitute into the equation 3.7. Therefore, we can apply this maximum load for design the MEMS switches.

CHAPTER 4

CONCLUSIONS

The main objective of this research was to overcome the mechanical and chemical problems of the liquid mercury MEMS switches by developing a method to produce structures of Gallium and Tin that can be used as MEMS switches. To understand the behavior of Ga and Sn micro-droplets, the droplets were deposited on W targets by an electroplating processing. The behavior was investigated by characterizing the structure, adhesion, hardness, and electrical performance of the droplets in MEMS structures. The results are as follows.

(1) The electroplated Sn was affected by the SiO_2 hole size, and the distance the Sn must move to reach the W surface, but the W spot size was not the main effect. The amount of Sn on W spots in the 0.1mm SiO_2 holes was greater than 0.2mm SiO_2 holes for the same size W target. For Sn, the target should be close in size to the field.

(2) Thermal reflow time affected the amount of reacted Sn with W. As the thermal reflow time increases, more Sn moves into the W dot. However, all times were likely too long for use in most devices.

(3) It was determined that the size of the SiO_2 hole, and the thermal reflow time and temperature were the main factors that affect the morphology of Ga droplets. The condition of electroplated Ga droplets in the large SiO_2 hole size (0.2 mm) was more uniform than in the small SiO_2 holes (0.1mm) which is the opposite of what was observed on the Sn. The surface shape of Ga was smooth after thermal reflow, and the small Ga droplets combined with each other as reflow time and temperature were increased.

However, there was only slight reflow of Ga droplets to the inside of the W spot as was expected after thermal reflow, suggesting that Ga may not be viable as a “healing” switch. Small droplets of Ga did reflow to large droplets, but for smaller size structures no preference between the W and SiO_2 surfaces was observed.

(4) It was revealed that the Ga droplet had good adhesion with the W target. The contact angles of deposited Ga droplets were $72^\circ \pm 5^\circ$and $64^\circ \pm 5^\circ$ when the height of Ga was less than the diameter of the W target. However, when the Ga droplet was deposited beyond the amount needed to cover the W target, approached a non-wetting condition.

(5) It was shown that the Ga droplet had low resistivity ($(1.128 \pm 0.6) \times 10^{-5}\ \Omega$ cm), and the value matched the theoretical value for Ga. The current device resistance is dominated by the Boron doped Si, and in a revised device would need to be lowered.

(6) It was exhibited that the hardness of the Ga droplet was an average of 17.2 HV, suggesting that the maximum applied stress that can be applied to a Ga droplet in a MEMS device is 60 MPa. The maximum applied load was calculated to $77 \pm 15\ \mu$N with the elastic modulus and the radius of the Ga, and the maximum applied stress. Therefore, we can apply the maximum load for design the MEMS switches.

REFERENCES

[1] K. Petersen, “Silicon as a mechanical material,” Proceedings of the IEEE, Vol. 70, No. 5, May 1982, pp. 420-457.

[2] M. Sakata, “An electrostatic microactuator for electro-mechanical relay,” Proceedings of the Tech Digest IEEE Micro Electro Mechanical Systems, Salt Lake City, UT, USA, February 1989, pp. 149-151.

[3] S. Roy, and M. Mehregany, “Fabrication of electrostatic nickel microrelays by nickel surface micromachining,” Proceeding of the IEEE MEMS Workshop, Amsterdam, The Netherlands, January-February 1995, pp. 353-357.

[4] E. Hashimoto, Y. Uenishi, and A. Watabe, “Thermally controlled magnetization microrelay,” Proceeding of the International Conference on Solid-State Sensors and Actuators, Stockholm, Sweden, June 1995, pp. 361-364..

[5] E.A. Sovero, R. Mihailovich, D.S. Deakin, J.A. Higgins, J.J. Yao, J.F. Denatale, and J.H. Hong, “Monolithic GaAs PHEMT MMICs integrated with high performance MEMS microrelays,” Proceeding of the SBMO/IEEE MTTT-S IMOC’99, Vol. 1, Rio de Janeiro, Brazil, August 1999, pp. 257-260.

[6] J. Kim, W. Shen, L. Latorre, and C.J. Kim, “A micromechanical switch with electrostatically driven liquid-metal droplet,” Sensors and Actuators, Vol. A 97-98, 2002, pp. 672-679.

[7] J. Simon, “A micromechanical relay with moving mercury micro-drop,” Ph.D. Dissertation, Mechanical and aerospace engineering department, University of California, Los Angeles, 1998.

[8] D. Hyman and M. Mehregany, “Contact physics of gold microcontacts for MEMS

Switches," IEEE Transactions on Components and Packaging Technology, Vol. 22, No.3, September 1999, pp.357-364.

[9] G.M. Rebeiz, J.B.Muldavin, "RF MEMS switches and switch circuits," IEEE Microwave magazine, December 2001, pp. 59-71.

[10] State Research of Russia Central R&D Institute of Robotics and Technical Cybernetics (http://www.rtc.ru/mems/nanotrubk-en.shtml).

[11] A. Christensen, "Fabrication and characterization of a liquid-metal micro-droplet thermal switch," MS thesis, Washington State University, 2003.

[12] T. D. Truong, "Selective deposition of micro scale liquid gallium alloy droplets," MS thesis, University of California Los Angeles, 2000.

[13] K. Crain, "Mechanical characterization and thermal modeling of a MEMS thermal switch," MS thesis, Washington State University, 2005.

[14] L.T. Taylor, J. Rancourt, and C.V. Perry, "Electrical Switches and sensors which use a non-toxic liquid metal composition," United States Patent Number 5478978, 1995.

[15] P.D.L. Breteque, "Gallium," Industrial and Engineering Chemistry, Vol. 56 No.6, June 1964, pp. 54-55.

[16] Lentech Periodic table (http://www.lenntech.com/periodic-chart.htm).

[17] I..A. Sheeka, I.S. Chaus, and T.T. Mityureva, "The chemistry of gallium," Elsevier Publishing Company, Amsterdam/ London/ New York, 1966.

[18] R.N. Lyon, "Liquid Metals Handbook," Atomic Energy Commission, Dept. of the Navy, Washington D.C., 1952

[19] W.G. Maffatt, "The handbook of binary phase diagrams," Genium Publishing

Corporation, New York, 1984.

[20] J. Simon, S. Saffer, and C.J. Kim, "IEEE Micro Electro Mechanical Systems (MEMS)," 1996, pp. 515-520.

[21] Webelements periodic table (http://www.webelements.com)

[22] ASTM B 374

[23] F.A. Lowenheim, "Electroplating," McGraw-Hill, New York, 1978.

[24] D.R. Askeland, "The science and engineering of materials," PWS Publishing Company, Boston, 1994.

[25] M.Madou, "Fundamentals of Microfabrication," CRC Press, New York, 1997.

[26] Instituto de Ciencia de Materiales de Madrid (ICMM), (http://www.icmm.csic.es/fis/english/evaporacion.html).

[27] UIUC Microelectonics Laboratory, "Solder conformity on wettable pads" (http://yoda.ccsm.uiuc.edu/research/hsieh/conformity.html).

[28] Printing Thick Film Hybrids, "Fundamentals of screen printing" (http://www.g-e-m.com/info/hybrid/hybrid2.html).

[29] Microfab Inc. Technical Note 99-01 "Background on Ink-Jet Technology," 1104 Summit Avenue, Plano, TX, 75074.

[30] Microfab Corporation, "Solder Jet Printing" (http://www.microfab.com).

[31] N.K. Adam, "The physics and chemistry of surfaces," Dover Publications, New York, 1968.

[32] M. J. Jaycock and G.D. Parfitt, "Chemistry of interfaces," Ellis Horwood Limited, England, 1981.

[33] M. Brugnara, "Using the ESEM for the measurement of contact angles on flat

samples," Microscopy and analysis, May 2007, pp. 9-11.

[34] L. Courbin and H. A. Stone, "Your wetting day," Physics Today, February 2007, pp. 84-85

[35] S. Yoshizawa, "Mechanical and chemical stability of adhered mercury droplets for a MEMS thermal switch," MS thesis, Washington State University, May 2006.

[36] J.C. Berg, "Wettability-Surfactant Science Series Vol. 49, Marcel Dekker Inc., New York, 1993.

[37] D.F. Bahr, J.W. Hoehn, N.R. Moody, W.W. Gerberich, "Adhesion and acoustic emission analysis of failures in nitrde films with a metal overlayer," Acta Mater 45, 1997, pp. 5163-5175.

[38] M.J. Cordill, "Adhesion of thin ductile films using stressed overlayers and nanoindentation," MS thesis, Washington State University, 2003.

[39] S. Kasap, "Semiconductor device fabrication," Special custom published e-booklet (http:// Materials.Usask.Ca), V.1.0, 1990-2001, pp. 1-18.

[40] K. Williams, K. Gupra, and M. Wasilik, "Etch rates for micromachining processing-part II," J. of Microelectromechanical Systems, Vol. 12, No. 6, December 2003, pp.761-778.

[41] D.A. Jones, "Principles and prevention of Corrosion," Prentice-Hall, New Jersey, 1996.

[42] S. Sundararajan and T.R. Bhat, "The electrodeposition of gallium from a chloride bath," J. of the Less-Common Metals, Vol. II, 1966, pp. 360-364.

[43] A.K. Graham, "Electroplating engineering handbook," Van Nostrand Reinhold Company, New York, 1971.

[44] Scion Corp. (http://www.scioncorp.com).

[45] R.S. Figliola and D.E. Beasley, “Theory and design for mechanical measurements,” John Wiley & Sons, New Jersey, 2006.

[46] M.Y. Ghannam and R. W. Dutton, “Resistivity of boron-doped polycrystalline silicon,” American Institute of Physics, Lett. 52(15), 11 April 1988, pp. 1222-1224.

[47] G.E. Dieter, “ Mechanical Metallurgy,” McGraw-Hill Book Company, London, 1988.

[48] M.A. Meyers and K.K. Chawla, “ Mechanical metallurgy,” Prentice-Hall, New Jersey, 1984.